AD_____

GRANT NO: DAMD17-93-J-3003

TITLE: WAVELET REPRESENTATIONS FOR DIGITAL MAMMOGRAPHY

PRINCIPAL INVESTIGATOR: Andrew F. Laine, D.Sc.

CONTRACTING ORGANIZATION: University of Florida
219 Grinter Hall
Gainesville, Florida 32611

REPORT DATE: December 15, 1994

TYPE OF REPORT: Annual

PREPARED FOR: U.S. Army Medical Research and Materiel Command
Fort Detrick
Frederick, Maryland 21702-5012

REPORT DOCUMENTATION PAGE

Form Approved
OMB No. 0704-0188

1. AGENCY USE ONLY (Leave blank)	2. REPORT DATE	3. REPORT TYPE AND DATES COVERED
	December 15, 1994	Annual, Nov. 16, 1993 - Nov. 15, 1994

4. TITLE AND SUBTITLE

Wavelet Representations for Digital Mammography

5. FUNDING NUMBERS

G: DAMD17-93-J-3003

6. AUTHOR(S)

Dr. Andrew F. Laine

7. PERFORMING ORGANIZATION NAME(S) AND ADDRESS(ES)

University of Florida
219 Grinter Hall
Gainesville, FL 32611

8. PERFORMING ORGANIZATION REPORT NUMBER

4514131

9. SPONSORING / MONITORING AGENCY NAME(S) AND ADDRESS(ES)

U.S. Army Medical Research and Materiel Command
Fort Detrick
Fredrick, MD 21702-5012

10. SPONSORING / MONITORING AGENCY REPORT NUMBER

11. SUPPLEMENTARY NOTES

Prepared in collaboration with: Walter Huda, Ph.D., Janice Honeyman, Ph.D., and Barbara Steinbach, MD.

12a. DISTRIBUTION / AVAILABILITY STATEMENT

Approved for public release; distribution unlimited.

12b. DISTRIBUTION CODE

13. ABSTRACT *(Maximum 200 words)*

This report describes recent progress in the development of a methodology for accomplishing adaptive contrast enhancement by multiscale representations. Our studies demonstrate that features extracted from multiresolution representations can provide an adaptive mechanism for the local emphasis of salient and subtle features of importance to mammography.

We establish connections between enhancement techniques based on dyadic wavelet analysis and traditional unsharp masking and prove that two cases of linear enhancement are mathematically equivalent to traditional unsharp masking with Gaussian low-pass filtering. In addition, a digital image editor is described that allows radiologists to interactively indicate on computer screens (simultaneously displaying four views) regions diagnosed as probable cancer. Construction of average interpolation wavelets and Deslauriers-Dubuc representations on an interval provide radiologiest with an interactive capability to process only suspicious regions and significantly reduce execution time. These representations (of arbitrary shape) provide improved sensitivity for the local emphasis of such features of importance to mammography including masses, spicules and microcalcifications. Finally, we report on the development of objective ways to assess the performance of wavelet image processing algorithms. Our objectives are to develop techniques to evaluate wavelet algorithms so they can then be optimized for clinical use in mammography.

14. SUBJECT TERMS	15. NUMBER OF PAGES
Mammography, Wavelet Analysis, Contrast enhancement, Multiscale representations, Digital image processing.	16. PRICE CODE

17. SECURITY CLASSIFICATION OF REPORT	18. SECURITY CLASSIFICATION OF THIS PAGE	19. SECURITY CLASSIFICATION OF ABSTRACT	20. LIMITATION OF ABSTRACT
Unclassified	Unclassified	Unclassified	Unlimited

FOREWORD

Opinions, interpretations, conclusions and recommendations are those of the author and are not necessarily endorsed by the US Army.

N/A Where copyrighted material is quoted, permission has been obtained to use such material.

N/A Where material from documents designated for limited distribution is quoted, permission has been obtained to use the material.

N/A Citations of commercial organizations and trade names in this report do not constitute an official Department of Army endorsement or approval of the products or services of these organizations.

____ In conducting research using animals, the investigator(s) adhered to the "Guide for the Care and Use of Laboratory Animals," prepared by the Committee on Care and Use of Laboratory Animals of the Institute of Laboratory Resources, National Research Council (NIH Publication No. 86-23, Revised 1985).

N/A For the protection of human subjects, the investigator(s) adhered to policies of applicable Federal Law 45 CFR 46.

____ In conducting research utilizing recombinant DNA technology, the investigator(s) adhered to current guidelines promulgated by the National Institutes of Health.

____ In the conduct of research utilizing recombinant DNA, the investigator(s) adhered to the NIH Guidelines for Research Involving Recombinant DNA Molecules.

____ In the conduct of research involving hazardous organisms, the investigator(s) adhered to the CDC-NIH Guide for Biosafety in Microbiological and Biomedical Laboratories.

Accesion For	
NTIS CRA&I	X
DTIC TAB	☐
Unannounced	☐
Justification	
By	
Distribution /	
Availability Codes	
Dist	Avail and / or Special
A-1	

Andrew F. Laine 12/13/94

PI - Signature Date

Contents

List of Figures

1 Introduction

Screen/film mammography is widely recognized as being the only effective imaging modality for the early detection of breast cancer in asymptomatic women [1]. Screening asymptomatic women using screen/film mammography has been shown to significantly reduce breast cancer mortality [2]. Breast cancer currently accounts for 32% of cancer incidence and 18% of cancer mortality for women in the United States. There were 182,000 new cases of breast cancer in the United States in 1993 and 46,000 deaths. Five year survival rates are generally very high (93%) for breast cancer staged as being localized, falling to 72% for regional disease and only 18% for distant disease [3]. The early detection of breast cancer is clearly a key ingredient of any strategy designed to reduce breast cancer mortality.

Major advances in screen/film mammography have occurred over the past decade [4] which have resulted in significant improvements in image resolution and film contrast. Of major importance is that these improvements have been achieved at reduced radiation doses. Despite these advances, however, screen/film mammography remains a diagnostic imaging modality where image interpretation remains very difficult. Breast radiographs are generally examined for the presence of malignant masses and indirect signs of malignancy such as the presence of microcalcifications and skin thickening. Unfortunately, it is unlikely that major improvements in imaging performance will be achieved by technical advances in screen/film radiography alone.

The major reason for poor visualization of small malignant masses is the minor difference in x-ray attenuation between normal glandular tissues and malignant disease [5]. This fact makes the detection of small malignancies problematical, especially in younger women who have denser breast tissue. Although calcifications have high inherent attenuation properties, their small size also results in a low subject contrast [6]. As a result, the visibility of small tumors, and any associated microcalcifications, will always be a problem in mammography as it is currently performed using analog film.

Improvements in the ability of screen/film mammography to detect small tumors and microcalcifications is more likely to occur by improving the visibility of these features. It has been suggested that as normally viewed, mammograms display only about 3% of the information they detect! [7].

Our approach to feature analysis and classification is motivated in part by recently discovered biological mechanisms of the human visual system [8]. Both multiorientation and multiresolution are known features of the human visual system. There exist cortical neurons which respond specifically to stimuli within certain orientations and frequencies.

In this report we describe exciting new results accomplished during our second year of study. In addition, we have continued our efforts in the development of wavelet transforms that exploit orientation and frequency selectivity to make mammographic features more obvious through localized contrast gain. Below, we describe in executive summary, recent accomplishments made in four subtask areas of our research and development project. The methodology, approach and experimental studies are reported in detail in the body of this report.

1.1 Overview of Contents

Contrast enhancement by multiscale nonlinear operators.

We first present a systematic approach to accomplish image contrast enhancement by multiresolution representations of the dyadic wavelet transform. This work expands upon our initial algorithms development during the first year of our investigation. We formulate two examples in which a linear enhancement operator is shown mathematically equivalent to traditional unsharp masking with a Gaussian low-pass filter. A formal analysis of wavelet filter selection and associated artifacts is carried out. We show that transform coefficients, modified within each level of scale by nonlinear operators, can make more obvious unseen or barely seen features. In addition, we introduce an edge-preserved denoising stage based on wavelet shrinkage with adaptive thresholding, and demonstrate that noise suppression and contrast enhancement can be achieved simultaneously within the same framework.

An interactive tool for editing digital mammograms.

The second section of our report describes the design and functionality of XMam, a computer image editor that allows radiologists to indicate on digitized mammograms regions considered as having signs of cancer. This is accomplished interactively on the computer screen by enclosing suspicious regions on the digitized images with polygons.

The purpose of this tool is to develop a database of cases diagnosed with cancer based on mammographic screening, and later confirmed or denied as positive by biopsy. This shall allow us to compile a large number of positive, borderline (difficult to diagnose) and negative cases and provide ground truth for the development and verification of our computer algorithms for the detection of breast cancer.

Local feature analysis via interval wavelets.

This section of the report introduces a novel approach for accomplishing interactive feature analysis by overcomplete multiresolution representations. Traditional wavelets adapted to "life on an interval", can overcome "edge effects" of wavelet representations on

a line. Methods of contrast enhancement are described based on two overcomplete multiresolution representations (interval wavelets): (1) Deslauriers-Dubuc interpolation, (2) Average interpolation.

We show quantitatively that transform coefficients, modified by an adaptive non-linear operator, can make more obvious unseen or barely seen features of mammography without requiring additional radiation.

Arbitrary regions of interest (ROI) of a mammogram are enhanced by average interpolation (AI) and Deslauriers-Dubuc interpolation (DD) representations on an interval. The results of local (ROI) enhancement and global enhancement of mammographic features are compared quantitatively. We demonstrate that our method can provide radiologists with an interactive capability to support high-speed localized processing of selected (suspicious) areas (lesions).

These results augment our preliminary findings accomplished during the first year of our study, and further demonstrate that features extracted from multiscale representations can provide an adaptive mechanism for accomplishing local contrast enhancement. In addition, we show that interval wavelet processing can be carried out in real-time (at video frame rates) over selected areas of arbitrary shape. This is significant in consideration of the large image matrix sizes produced by digital detectors. By improving the visualization of breast pathology we can improve chances of early detection while requiring less time to evaluate mammograms for most patients.

Quantitative evaluation of clinical images.

The final section of our report relates to the development of objective ways to assess the performance of wavelet image processing algorithms. The objective is to develop techniques to evaluate wavelet algorithms so they can then be optimized for clinical use in mammography.

Substantial progress has been made in the development of techniques to assist in the quantitative evaluation of wavelet based image processing algorithms. In addition, these techniques have been applied to optimize the three parameters available in current wavelet based algorithms. Specific achievements in the past year include:

- a demonstration of the ability of optimized wavelet based algorithms to make visible simple objects in a noisy background which were previously invisible;

- a demonstration of the inherent superiority of wavelet based algorithms for the detection of simple objects as compared to algorithms frequently used in medical imaging including unsharp mask enhancement and median filtering;

- a demonstration of the special requirements of wavelet algorithms when enhancing the visibility of features of specific interest in mammography, namely microcalcifications, masses and fibril structures.

In the next section, we shall describe in detail our wavelet processing algorithms, experimental methods and example results obtained. In addition, we list and summarize publications and presentations made by our researchers during the past year of our investigation.

2 Body

2.1 Contrast Enhancement by Multiscale and Nonlinear Operators

2.1.1 Introduction

Image enhancement techniques have been widely used in radiology, where subjective quality of images is important for reliable diagnosis. Image contrast is a important factor in subjective quality. Many algorithms for contrast enhancement have been proposed. A comprehensive survey is presented in reference [9]. Among them, histogram modification and edge enhancement techniques are most commonly used.

Histogram modification techniques [10, 11] are attractive due to their simplicity and speed, and have achieved acceptable results for some applications. In general, a transformation function is derived from a desired histogram and the histogram of an input image. Note that the transformation function is in general nonlinear. For continuous functions, an information lossless transformation may be achieved. However, for digital images with a finite number of gray levels, such a transformation results in information loss, due to quantization errors. For example, a subtle edge may be merged with its neighboring pixels and disappear. Attempts to incorporate local context into the transformation process have not been fruitful. For example, simple adaptive histogram equalization [12] with a fixed contextual region (window) cannot adapt to features of distinct sizes.

Most edge enhancement algorithms share a common strategy implicitly: edge detection and subsequent "crispening". "Unsharp masking" sharpens edges by subtracting a portion of a Laplacian filtered component from an original image. This technique was justified as an approximation of a deblurring process in [13]. Loo *et al.* [14] studied a extension of this technique in the context of radiographs. Another extension based on Laplacian filtering was proposed in [15]. However, these (unsharp masking) techniques remain limited by their linear and single scale properties, and are less effective for images containing wide range of features such as mammography. In an attempt to overcome these limitations, a local contrast measure and nonlinear transform functions were introduced in [16], and subsequently refined in [17]. However, limitations remain in these nonlinear methods: (1) They operate on a single scale, (2) There is no explicit noise suppression stage (actually noise may be amplified significantly), and (3) Nonlinear transform functions were introduced ad-hoc without a rigorous mathematical analysis of their enhancement mechanisms.

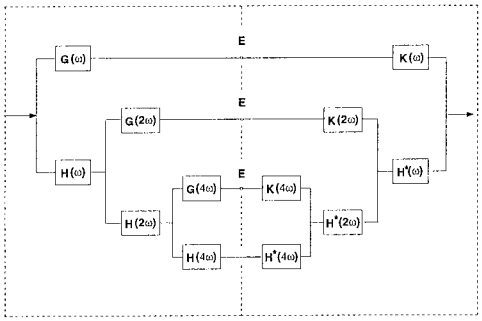

Figure 1: One dimensional discrete dyadic wavelet transform (three-level shown).

Recent advancement of wavelet theory has sparked researchers in the applications of image contrast enhancement [18, 19, 20, 21, 22, 23, 24]. These early studies showed promise, but remained at an experimental level. In this report, we give a detailed mathematical analysis of a dyadic wavelet transform, and reveal its connection to traditional technique of unsharp masking. In addition, we propose a simple nonlinear enhancement function and analyze the problem of artifacts. Moreover, we introduce an explicit denoising stage that preserves edges using wavelet shrinkage [25] with adaptive thresholding.

These techniques are described in the following sections: Section 2.1.2 presents a one dimensional dyadic wavelet transform. Section 2.1.3 analyzes linear enhancement and its mathematical connection to traditional unsharp masking. Section 2.1.4 analyzes a simple nonlinear enhancement by point-wise functional mapping. Section 2.1.5 introduces denoising with wavelet shrinkage and an adaptive approach for finding threshold values. Section 2.1.6 presents a two dimensional extension for digital mammography and special procedures developed for denoising and enhancement that avoid orientation distortions. Section 2.1.7 presents sample experimental results and comparisons. Finally, Section 2.1.8 concludes our discussion and proposes future research directions.

2.1.2 One dimensional discrete dyadic wavelet transform

A fast algorithm [26] for computing 1-D discrete dyadic wavelet transform (DDWT) is shown in Figure 1. The left side shows the structure of decomposition, and the right, reconstruction. For an N-channel structure, there are $N-1$ high-pass or band-pass channels and a low-pass channel. Thus, the decomposition of a signal produces $N-1$ sets of wavelet coefficients and a set of coarse signal.

Since a dyadic wavelet is not an orthogonal basis, there is no down-sampling and up-sampling shown in Figure 1, and its decomposition filters differ from its reconstruction

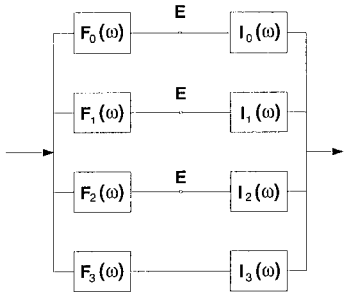

Figure 2: An equivalent multi-channel structure for three-level DDWT.

filters.

For simplicity of analysis, an equivalent multi-channel structure is shown in Figure 2. This computational structure also makes obvious the potential for parallel processing.

We shall refer to filters $F_m(\omega)$ and $I_m(\omega)$ in Figure 2 as forward filters and inverse filters, respectively. Their relationship to filters $G(\omega)$, $K(\omega)$ and $H(\omega)$ are explicitly given by

$$\begin{aligned} F_0(\omega) &= G(\omega), \quad F_N(\omega) = \prod_{l=0}^{N-1} H(2^l\omega), \\ F_m(\omega) &= \left[\prod_{l=0}^{m-1} H(2^l\omega)\right] G(2^m\omega), \ 1 \le m \le N-1. \end{aligned}$$

and

$$\begin{aligned} I_0(\omega) &= K(\omega), \quad I_N(\omega) = \prod_{l=0}^{N-1} H^*(2^l\omega), \\ I_m(\omega) &= \left[\prod_{l=0}^{m-1} H^*(2^l\omega)\right] K(2^m\omega), \ 1 \le m \le N-1. \end{aligned}$$

Since filters $H(\omega)$, $G(\omega)$ and $K(\omega)$ satisfy condition

$$\|H(\omega)\|^2 + G(\omega)K(\omega) = 1,$$

filters $F_m(\omega)$ and $I_m(\omega)$ completely cover the frequency domain,

$$\sum_l F_l(\omega)I_l(\omega) = 1.$$

Channel frequency responses $C_m(\omega)$ can be written as

$$C_m(\omega) = F_m(\omega)I_m(\omega) = \begin{cases} 1 - \|H(\omega)\|^2 & , \ m = 0, \\ \prod_{l=0}^{m-1} \left\|H(2^l\omega)\right\|^2 \left[1 - \|H(2^m\omega)\|^2\right] & , \ 1 \le m \le (N-1), \\ \prod_{l=0}^{N-1} \left\|H(2^l\omega)\right\|^2 & , \ m = N. \end{cases}$$

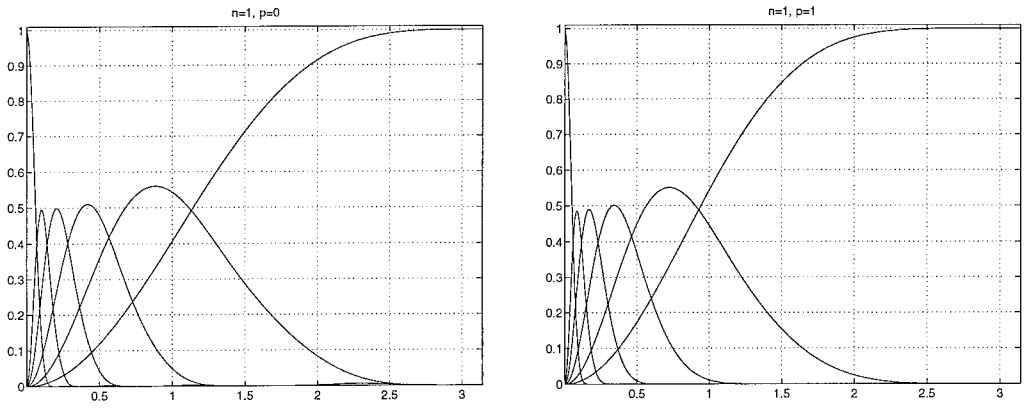

(a) (b)

Figure 3: Channel frequency responses for $N = 6, n = 1$ and (a) $p = 0$ and (b) $p = 1$.

As an example, we consider an extension of the class of filters proposed in [26]

$$H(\omega) = e^{jp\frac{\omega}{2}} \left[\cos\left(\frac{\omega}{2}\right)\right]^{2n+p}, \tag{1}$$

where $p = 0$, or 1. Let

$$\Theta_{m,q}(\omega) = \left[\prod_{l=0}^{m-1} \cos(2^{l-1}\omega)\right]^q,$$

then we can show that

$$\Theta_{m,q}(\omega) = \left[\frac{\sin(2^{m-1}\omega)}{2^m \sin(\frac{\omega}{2})}\right]^q, \tag{2}$$

and therefore

$$C_m(\omega) = \begin{cases} \Theta_{m,4n+2p}(\omega) - \Theta_{m+1,4n+2p}(\omega) & , \ 0 \le m \le (N-1), \\ \Theta_{N,4n+2p}(\omega) & , \ m = N. \end{cases} \tag{3}$$

Note that $\Theta_{0,n}(\omega) = 1$, and for $0 < m < N$,

$$C_m(\omega) = \Theta_{m,4n+2p}(\omega) - \Theta_{m+1,4n+2p}(\omega) = \sin^2\left(\frac{\omega}{2}\right) \ 4^m \Theta_{m,4n+2p+2}(\omega) \sum_{l=0}^{2n+p-1} \left[\cos\left(2^{m-1}\omega\right)\right]^{2l},$$

and $\sin^2\left(\frac{\omega}{2}\right)$ is the frequency response of the discrete Laplacian operator of impulse response $\{1, -2, 1\}$.

$\Theta_{m,q}(\omega)$ with even exponential q is approximate a Gaussian function, while the frequency responses of channels ($0 < m < N$) are approximate a Laplacian of Gaussian. Figure 3 shows the distinct channel frequency responses, and Figure 4 compares $\Theta_{2,4}(\omega)$ and $\Theta_{2,6}(\omega)$ with related Gaussians.

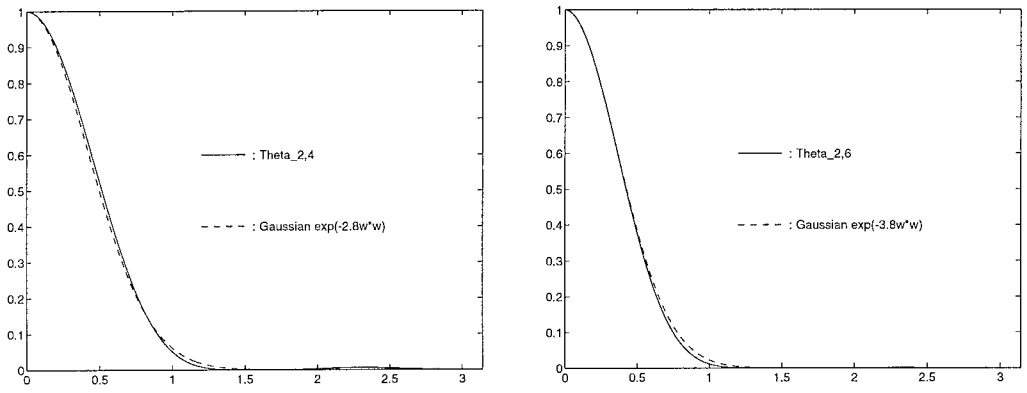

(a) (b)

Figure 4: (a) $\Theta_{2,4}(\omega)$ compared with the Gaussian function $e^{-2.8\omega^2}$.
(b) $\Theta_{2,6}(\omega)$ compared with the Gaussian function $e^{-3.8\omega^2}$.

2.1.3 Linear enhancement and unsharp masking.

Review of unsharp masking

A prototype of unsharp masking was defined [13] as

$$\tilde{s}(x,y) = s(x,y) - k\Delta s(x,y), \tag{4}$$

where $\Delta = \frac{\partial^2}{\partial x^2} + \frac{\partial^2}{\partial y^2}$ is the Laplacian operator. However, this original formula worked only at the level of finest resolution. More versatile formulas were later developed in two ways, described below.

One way to extend the original formula is based on exploiting the averaging concept behind the Laplacian operator. The discrete form of the Laplacian operator may be written as

$$\begin{aligned}\Delta s(i,j) &= [s(i+1,j) - 2s(i,j) + s(i-1,j)] + [s(i,j+1) - 2s(i,j) + s(i,j-1)] \\ &= -5\left\{s(i,j) - \frac{1}{5}[s(i+1,j) + s(i-1,j) + s(i,j) + s(i,j+1) + s(i,j-1)]\right\}\end{aligned}$$

This formula shows that the discrete Laplacian operator can be implemented by subtracting from the value of a central point its average neighborhood. Thus, an extended formula [14] can be written as

$$\tilde{s}(i,j) = s(i,j) + k\,[s(i,j) - s(i,j) * h(i,j)]\,, \tag{5}$$

where $h(i,j)$ is a discrete averaging filter, and $*$ denotes convolution. In [14], a equal-weighted averaging mask was used:

$$h(x,y) = \begin{cases} 1/N^2, & |x| < N/2, |y| < N/2 \\ 0, & \text{otherwise.} \end{cases}$$

Another way to extend the prototype formula [15] came from the idea of Laplacian-of-Gaussian filter, which expands Equation (4) into

$$\tilde{s}(x,y) = s(x,y) - k\Delta\left[s(x,y) * g(x,y)\right] = s(x,y) - k\left[s(x,y) * \Delta g(x,y)\right], \tag{6}$$

where $g(x,y)$ is an Gaussian function, and $\Delta g(x,y)$ is a Laplacian-of-Gaussian filter.

Finally, we mention here that both extensions shown in Equations (5) and (6) are limited to a single scale.

Inclusion of unsharp masking within DDWT framework

We shall prove that unsharp masking with a Gaussian lowpass filter is included in a dyadic wavelet framework for enhancement by considering two special cases of linear enhancement.

In the first case, transform coefficients of channels $0 \le m \le N-1$ are enhanced (multiplied) by the same gain $G_0 > 1$, or $G_m = G_0 > 1$, $0 \le m \le N-1$. The system frequency response is thus

$$\begin{aligned} V(\omega) &= \sum_{m=0}^{N-1} G_m C_m(\omega) + C_N(\omega) = G_0 \sum_{m=0}^{N} C_m(\omega) - (G_0 - 1)C_N(\omega) \\ &= G_0 - (G_0 - 1)C_N(\omega) = 1 + (G_0 - 1)\left[1 - C_N(\omega)\right]. \end{aligned}$$

The input-output relationship of the system is simply

$$\tilde{s}[i] = s[i] + (G_0 - 1)\left\{s[i] - s[i] * c_N[i]\right\}. \tag{7}$$

Since $C_N(\omega)$ is approximately a Gaussian lowpass filter, Equation (7) may be seen as a 1-D counterpart of Equation (5).

In the second case, transform coefficients of a single channel p, $0 \le p < N$ are enhanced (multiplied) by a gain $G_p > 1$, thus

$$V(\omega) = \sum_{m \ne p} C_m(\omega) + G_p C_p(\omega) = \sum_{m=0}^{N} C_m(\omega) + (G_p - 1)C_p(\omega) = 1 + (G_p - 1)C_p(\omega). \tag{8}$$

Using the filter class of Equation (1), the input-output relationship of the system (8) can be written as

$$\tilde{s}[i] = s[i] - (G_p - 1) \cdot \Delta\left\{s[i] * \beta[i]\right\}, \tag{9}$$

where $\beta[i]$ is the impulse response of an approximate Gaussian filter. Similarly, Equation (9) may be seen as a 1-D counterpart of Equation (6).

The inclusion of these two forms of unsharp masking clearly demonstrates the flexibility and versatility of a dyadic wavelet framework.

2.1.4 Nonlinear enhancement by functional mapping

Linear enhancement can be seen as a mapping of wavelet coefficients by a linear function $E_m(x) = G_m x$. Therefore, a direct extension of the linear enhancement is a nonlinear mapping function $E_m(x)$.

For linear enhancement, selection of filters $G(\omega)$ (and thus $K(\omega)$) made no difference. However, we shall see that the selection of filters is critical for the nonlinear case.

Nonlinear enhancement I: Laplacian filter.

A discrete Laplacian operator can be implemented by the filter

$$G(\omega) = -4\left[\sin\left(\frac{\omega}{2}\right)\right]^2, \quad \text{or} \quad g[n] = \{1, -2, 1\},$$

such that $g[n] * s[n] = s[n+1] - 2s[n] + s[n-1]$.

In addition, both filters $H(\omega)$ and $K(\omega)$ can also be symmetric,

$$H(\omega) = \left[\cos\left(\frac{\omega}{2}\right)\right]^{2n}$$

and

$$K(\omega) = \frac{1 - \|H(\omega)\|^2}{G(\omega)} = -\frac{1}{4}\sum_{l=0}^{2n-1}\left[\cos\left(\frac{\omega}{2}\right)\right]^{2l}.$$

Both forward and inverse filters ($0 \le m \le N-1$) can be derived as

$$F_m(\omega) = -4\left[\sin(2^{m-1}\omega)\right]^2 \Theta_{m,2n}(\omega) = -4\sin^2\left(\frac{\omega}{2}\right) 4^m \Theta_{m,2n+2}(\omega) = G(\omega)\Lambda_m(\omega) \quad (10)$$

and

$$I_m(\omega) = -\Theta_{m,2n}(\omega)\frac{1}{4}\sum_{l=0}^{2n-1}\left[\cos\left(2^{m-1}\omega\right)\right]^{2l} = -\Gamma_m(\omega).$$

Note that the forward filters $F_m(\omega)$ ($0 < m < N$) can be interpreted as two cascaded operations, a Gaussian averaging of $\Theta_{m,2n+2}(\omega)$ and the Laplacian of $-4\left[\sin(\frac{\omega}{2})\right]^2$, while the set of inverse filters $I_m(\omega)$ are low-pass filters. In this case, wavelet coefficients may be written simply as

$$w_m[i] = \Delta\{s[i] * \lambda_m[i]\}$$

where Δ is the discrete Laplacian operator, and $\lambda_m[i]$ is approximately a Gaussian filter. This means that each wavelet coefficient $w_m[i]$ is dependent on the local contrast of the original signal at i.

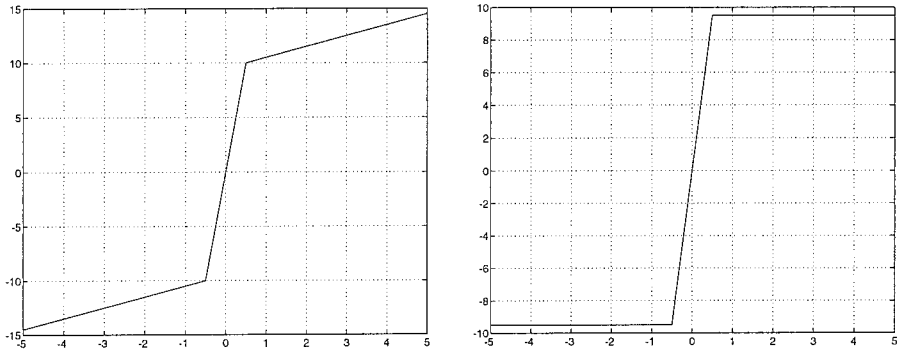

(a) (b)

Figure 5: (a) $E(x)$ and (b) $\delta(x)$, both with $T = 0.5$ and $K = 20$.

The basic guidelines for designing a nonlinear enhancement function are:

(1) An area of low contrast should be enhanced more than an area of high contrast. This is equivalent to saying that small values of $w_m[i]$ should have larger gains.

(2) A sharp edge should not be blurred.

Such functions may be further subjected to the constraints of:

(1) Monotonicity, in order not to change the position of local extrema, nor create new extrema, and

(2) Antisymmetry, $E(-x) = -E(x)$, in order to preserve phase polarity for "edge crispening".

A simple three-segment function that satisfies these conditions is shown in Figure 5,

$$E(x) = \left\{ \begin{array}{ll} x - (K-1)T & , \text{ if } x < -T \\ Kx & , \text{ if } |x| \leq T \\ x + (K-1)T & , \text{ if } x > T \end{array} \right\} = x + \delta(x) \tag{11}$$

where $K > 1$ and

$$\delta(x) = \left\{ \begin{array}{ll} -(K-1)T, & \text{if } x < -T, \\ (K-1)x, & \text{if } |x| \leq T, \\ (K-1)T, & \text{if } x > T. \end{array} \right.$$

Thus, an enhanced signal can be written as

$$\begin{aligned} \tilde{s}[n] &= \sum_{m=0}^{N-1} E_m \left\{ s[n] * f_m[n] \right\} * i_m[n] + s[n] * f_N[n] * i_N[n] \\ &= \sum_{m=0}^{N} s[n] * f_m[n] * i_m[n] + \sum_{m=0}^{N-1} \delta_m \left\{ \Delta \left(s[n] * \lambda_m[n] \right) \right\} * i_m[n] \end{aligned}$$

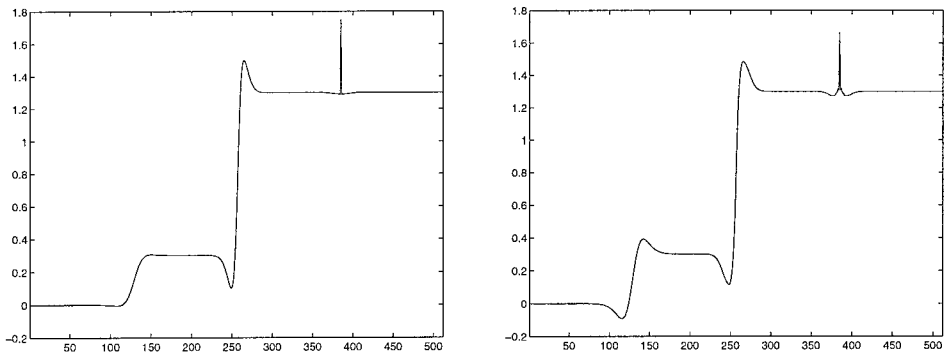

Figure 6: 1-D contrast enhancement by four-level dyadic wavelet analysis with (a) a linear operator with $K_0 = 2.3$, and (b) a nonlinear operator with $t = 0.1$ and $K_0 = 7$.

or,

$$\tilde{s}[n] = s[n] - \sum_{m=0}^{N-1} \delta_m \left\{ \Delta \left(s[n] * \lambda_m[n] \right) \right\} * \gamma_m[n]. \tag{12}$$

We point out that the formula of Equation (12) can be seen as a multiscale and nonlinear extension of the original unsharp masking defined by Equation (6).

The enhancement operator δ_m has two free parameters: threshold T_m and gain K_m. In our experimental studies, $K_m = K_0$, $0 \leq m \leq N-1$, and $T_m = t \times \max\{|w_m[n]|\}$, where $0 < t \leq 1$ was user specified. For $t = 1.0$, wavelet coefficients at levels $0 \leq m \leq N-1$ will be multiplied by a gain of K_0, previously shown to be equivalent to unsharp masking. This means our nonlinear algorithm includes unsharp masking as a subset. Figure 6 shows a numerical example comparing linear and nonlinear enhancement. Note the lack of enhancement for the leftmost edge, for the case of the linear operator.

We argue that multiscale unsharp masking as defined by Equation (12) makes an marked improvement over traditional techniques in two respects:

1. The fast multiscale (or multimask) decomposition efficiently searches features existing in different scales, making a try-and-fail strategy of window selection unnecessary.

2. The nonlinear algorithm enhances small features in each scale without blurring edges of larger features, making simultaneous enhancement features of all sizes possible.

Furthermore, artifacts possibly created by a nonlinear enhancement operator can be limited by careful filter selection and constraints. For example, the arguments presented below assure that no new extrema will be created within each channel.

1. Filters are zero-phase. No spatial shifting exists in the transform space.

2. $E(x)$ is a monotonically increasing function (Such a mapping will not produce new extrema points. Since at point x_0, $E[f(x_0)]$ is an extrema if and only if $f(x_0)$ is an extrema).

3. The reconstruction filters are simply zero-phase smoothing filters.

Nonlinear enhancement II: gradient filter.

After analyzing the Laplacian filter, a natural question is, "Are there any other possible filters for $G(\omega)$?". The possible candidates are limited by the constraint $G(\omega)K(\omega) = 1 - \|H(\omega)\|^2$. For the class of filters defined by Equation (1), we can derive that

$$G(\omega)K(\omega) = \sin^2\left(\frac{\omega}{2}\right) \sum_{l=0}^{2n+p-1} \left[\cos\left(\frac{\omega}{2}\right)\right]^{2l}.$$

As a result, the only other meaningful choice of filter $G(\omega)$ appears to be a gradient operator

$$G(\omega) = 2je^{-j\frac{\omega}{2}} \sin\left(\frac{\omega}{2}\right), \text{ or, } g[0] = 1, g[1] = -1, \tag{13}$$

such that $g[i] * s[i] = s[i] - s[i-1]$. The reasoning comes from the fact that derivatives higher than two have more than two local extrema for a soft edge. Therefore, nonlinear enhancement of derivatives higher than two may produce additional edges (artifacts).

For the gradient filter $G(\omega)$, we selected the filter

$$H(\omega) = e^{j\frac{\omega}{2}} \left[\cos\left(\frac{\omega}{2}\right)\right]^{2n+1}$$

and accordingly

$$K(\omega) = -e^{j\omega}G(\omega) \frac{1}{4} \sum_{l=0}^{2n} \left[\cos\left(\frac{\omega}{2}\right)\right]^{2l}.$$

We then derived the forward filters

$$F_m(\omega) = G(\omega)2^m \Theta_{m,2n+2}(\omega) = G(\omega)\Lambda_m(\omega)$$

and inverse filters

$$I_m(\omega) = -e^{j\omega}G(\omega)\Gamma_m(\omega),$$

where

$$\Gamma_m(\omega) = 2^m \Theta_{m,2n+2}(\omega) \frac{1}{4} \sum_{l=0}^{2n} \left[\cos\left(2^{m-1}\omega\right)\right]^{2l}$$

is a low-pass filter.

In this case, the associated wavelet coefficients may be written as

$$w_m[n] = \nabla^- \{s[n] * \lambda_m[n]\}$$

where ∇^- is a discrete *backward* gradient operator characterized by $\nabla^- s[n] = s[n] - s[n-1]$.

Finally, the enhanced signal may be written as

$$\tilde{s}[n] = -\sum_{m=0}^{N-1} \nabla^+ \left\{ E_m \left[\nabla^- \left(s[n] * \lambda_m[n] \right) \right] \right\} * \gamma_m[n] + s[n] * \lambda_N[n] * \gamma_N[n] \tag{14}$$

where ∇^+ is a discrete *forward* gradient operator characterized by $\nabla^+ s[n] = s[n+1] - s[n]$, corresponding to $e^{j\omega} G(\omega)$ in $I_m(\omega)$.

For the sake of discussing artifacts, let us consider the channel output of an enhanced signal

$$\nabla^+ \left\{ E_m \left[\nabla^- \left(s_m[n] \right) \right] \right\} * \gamma_m[n]$$

where $s_m[n] = s[n] * \lambda_m[n]$ and $\gamma_m[n]$ is a zero-phase low-pass filter. The suspicious part is

$$\nabla^+ \left\{ E_m \left[\nabla^- \left(s_m[n] \right) \right] \right\},$$

with its continuous counterpart being

$$\frac{d}{dx} \left\{ E \left[\frac{d}{dx} s_m(x) \right] \right\} = E' \left[s'_m(x) \right] s''_m(x) = \alpha \left[s'_m(x) \right] s''_m(x),$$

where $\alpha(x) = E'(x)$ can be seen as a gain for $s''_m(x)$. Note that gain α is based on $s'_m(x)$ instead of $s''_m(x)$.

The proof below shows that only a linear function $E(x) = Gx$ (corresponding to unsharp masking) can guarantee that positions of extrema of $s''_m(x)$ remain unchanged.

Proof. Let $u(x) = \alpha \left[f'(x) \right] f''(x)$, then $u'(x) = \alpha'(f')(f'')^2 + \alpha(f') f'''$. At extrema point x_0 of f'' , $f'''(x_0) = 0$, thus $u'(x_0) = \alpha' \left[f'(x_0) \right] \left[f''(x_0) \right]^2$. We consider a particular signal of a soft edge, $f(x) = 1/(1 + e^{-2\beta x})$, for which $f'(x) = \beta / \left[2\cosh^2(\beta x) \right]$, $f''(x) = -\beta^2 \sinh(\beta x) / \cosh^3(\beta x)$ and $f'''(x) = -\beta^3 \left[1 - 2\sinh^2(\beta x) \right] / \cosh^4(\beta x)$. Local extrema points x_0 satisfy $1 - 2\sinh^2(\beta x_0) = 0$, $f'(x_0) = \beta/3$ and $\left[f''(x_0) \right]^2 = 4\beta^4/27$. For all $\beta \neq 0$, $f'(x_0) \neq 0$ and $\left[f''(x_0) \right]^2 \neq 0$. Therefore, in order for $u'(x_0) = 0$, the function $\alpha'(x)$ must satisfy $\alpha' \left[f'(x_0) \right] = \alpha'(\beta/3) = 0, \forall \beta$. That is $\alpha(x) = constant$, or $E(x) = Gx$.

Change in position of extrema points may result in *undesirable distortion* or *artifacts*. Figure 7 shows an example of shifting caused by a hyperbolic enhancement function

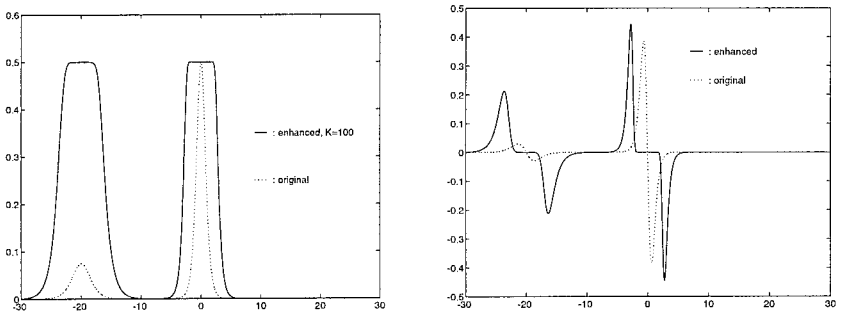

(a) (b)

Figure 7: (a) $E\left[s'_m(x)\right]$ overlayed with $s'_m(x)$ (b) $\alpha\left[s'_m(x)\right] s''_m(x)$ overlayed with $s''_m(x)$.

$E(x) = A \cdot \tanh(Kx)$ with $K = 100$. For other nonlinear functions, new local extrema may also be created.

Intuitively, the problem associated with the gradient filter is due to high-pass filtering in reconstruction. The significance of this analytical result suggests that this nonlinear approach may not be appropriate for other wavelet bases if their reconstruction (inverse) involves high-pass filtering.

2.1.5 Noise-suppressed enhancement

A structure for combined denoising and enhancement

The nonlinear enhancement methods proposed previously did not take into account the presence of noise. In general, noise exists in a digitized image, due to the imaging device and quantization. As a result of nonlinear processing, noise may be amplified and may diminish the benefits of an enhancement.

Unfortunately, denoising is a very difficult problem for two reasons. Fundamentally, there is no absolute boundary to distinguish a feature from noise. Even if there are known characteristics of a certain type of noise, it may be theoretically impossible to completely separate the noise from features of interest. Therefore, most denoising methods may be seen as ways to suppress very high frequency and incoherent components of an input signal.

A very simple method of denoising that is equivalent to low-pass filtering is naturally included in our dyadic wavelet framework. That is, simply discard several channels of highest resolution, and enhance channels confined to lower frequency. The problem associated with this linear denoising approach is that edges are blurred significantly, and is thus not suitable within a contrast enhancement scheme. Figure 10 (c) shows an example of this approach. In order to achieve edge-preserved denoising, more sophisticated methods based on a framework for wavelet analysis were proposed in the literature. Mallat and

Hwang [27] connected noise behavior to singularities. Their algorithm was based on a multiscale edge representation. The algorithm traced modulus wavelet maxima to evaluate local Lipschitz exponents and deleted maxima points with a negative Lipschitz exponent. Donoho [25] proposed nonlinear wavelet shrinkage. The algorithm shrinks wavelet coefficients towards zero based on a level-dependent threshold.

The wavelet shrinkage method can be trivially incorporated into our nonlinear enhancement framework by simply adding an extra segment to the enhancement function $E(x)$ of Equation (11).

$$E(x) = \begin{cases} x - (K-1)T_e + KT_n & , \text{ if } x \leq -T_e \\ K(x + T_n) & , \text{ if } -T_e \leq x \leq -T_n \\ 0 & , \text{ if } |x| \leq T_n \\ K(x - T_n) & , \text{ if } T_n \leq x \leq T_e \\ x + (K-1)T_e - KT_n & , \text{ if } x \geq T_e \end{cases} \tag{15}$$

However, there are two arguments which favor shrinking gradient coefficients instead of Laplacian coefficients.

First, gradient coefficients exhibit a higher signal to noise ratio (SNR). For any shrinkage scheme to be effective, an essential property is that the magnitude of a signal's components be larger than that of existing noise (most of time). It is thus sensible to define the SNR as the maximum magnitude of a signal over the maximum magnitude of noise. For example, consider a soft edge model $f(x) = A/(1 + e^{-2\beta x})$, $A > 0$. Its first and second derivatives are $f'(x) = A\beta/\left[2\cosh^2(\beta x)\right]$ and $f''(x) = -A\beta^2 \sinh(\beta x)/\cosh^3(\beta x)$, with magnitude of local extrema $|f'(x_0)| = A|\beta|/3$ and $|f''(x_0)| = 2A\beta^2/3\sqrt{3}$, respectively. By this simple model, we can reasonably assume that noise is characterized by relatively small A value and large β value. Clearly that gradient coefficients have a higher SNR than that of Laplacian coefficients because of less contribution of β. Figures 8 (b) and (c) show first and second derivatives, respectively, for an input signal (a) with two distinct edges.

Second, boundary contrast is not affected by shrinking gradient coefficients. As shown in Figure 8, coefficients aligned to the boundary of edges are the local extrema in the case of the first derivative (gradient), and zero crossings in the case of the second derivative (Laplacian). For a simple point-wise shrinking operator, there is no way to distinguish the B points from the A points. As a result, both regions around the B's and A's are shrunken, and the discontinuity in B will sacrifice boundary contrast.

In the previous section, we argued that nonlinear enhancement should be performed on Laplacian coefficients. Therefore, in order to incorporate denoising into our enhancement algorithm, we need to split the Laplacian operator into two cascaded gradient operators.

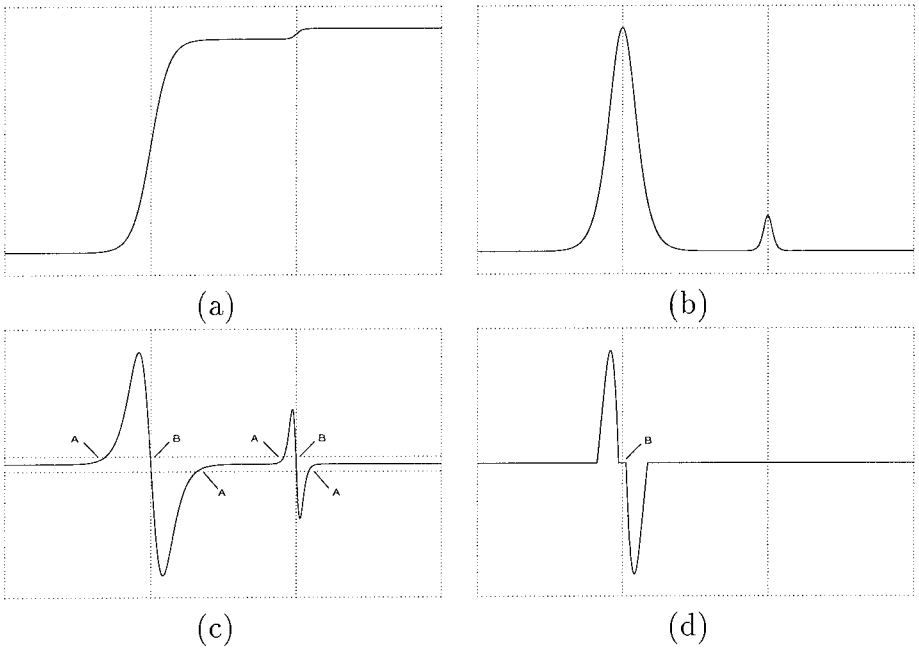

Figure 8: (a) Signal with two edges. (b) 1st derivative (gradient). (c) 2nd derivative (Laplacian). (d) Shrunken 2nd derivative.

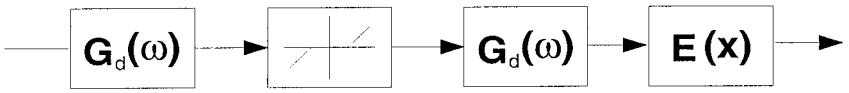

Figure 9: Incorporating wavelet shrinkage into an enhancement framework (level one shown).

Note that

$$G_m(\omega) = -4\left[\sin\left(2^{m-1}\omega\right)\right]^2 = \begin{cases} \left[e^{-j\omega/2}G_d(\frac{\omega}{2})\right]\left[e^{j\omega/2}G_d(\frac{\omega}{2})\right] & \text{, if } m=0, \\ \left[G_d(2^{m-1}\omega)\right]^2 & \text{, otherwise.} \end{cases} \tag{16}$$

where $G_d(\omega) = 2j\sin(\omega)$.

Denoising by wavelet shrinkage [25] can then be incorporated into this structure as illustrated in Figure 9, where the shrinking operator can be written as

$$C(x) = sign(x) \cdot \begin{cases} |x| - T_n & \text{, if } |x| > T_n, \\ 0 & \text{, otherwise.} \end{cases}$$

Note that the shrinking operator is a piece-wise linear and monotonically non-decreasing function. In practice, this will not introduce artifacts.

Finally, a denoised and enhanced signal can be written overall as

$$\tilde{s}[n] = -\sum_{m=0}^{N-1} E_m \left\{\nabla^+\left[C_m\left(\nabla^-\left(s[n] * \lambda_m[n]\right)\right)\right]\right\} * \gamma_m[n] + s[n] * \lambda_N[n] * \gamma_N[n].$$

Threshold estimation for denoising

The threshold T_n is a critical parameter in the shrinking operation. For a white noise model and orthogonal wavelet, Donoho [25] suggested a formula of $T_n = \sqrt{2\log(N)}\sigma/\sqrt{N}$, where N is the length of a input signal and σ is the standard deviation of wavelet coefficients. However, the dyadic wavelet we applied is not an orthogonal wavelet. Moreover, in our 2-D applications, a shrinking operation is applied to magnitudes of gradient coefficients instead of wavelet coefficients themselves. Therefore, the threshold estimation method proposed in [28] for edge detection may be more suitable.

In our shrinking operation, the magnitudes of the gradient of a Gaussian low-passed signal are modified. As pointed out in [28], for white Gaussian noise, the probability distribution function of the magnitudes of gradient is characterized by the Rayleigh distribution:

$$Pr_{\|\Delta f\|}(m) = \begin{cases} \frac{m}{\eta^2} e^{-(m/\eta)^2/2} & , m \geq 0, \\ 0 & , m < 0. \end{cases}$$

To estimate η, a histogram (probability) of $\|\Delta f\|$ was computed, and then iterative curve fitting was applied. Under this model, the probability p of noise removal for a particular threshold τ can be calculated [28] by

$$p = \frac{\int_0^\tau Pr_{\|\Delta f\|}(m)dm}{\int_0^\infty Pr_{\|\Delta f\|}(m)dm},$$

and thus $\tau = \sqrt{-2\ln(1-p)}\ \eta$. For $p = 0.999$, $\tau = 3.7\eta$.

Figure 10 compares different existing approaches. In (b), we observed that enhancement without any denoising results in annoying background noise. In (c), edges were smeared and broadened by low-pass-enhancement combination. Only in (d), with wavelet shrinkage, we were able to achieve the remarkable result of denoising and contrast enhancement simultaneously.

To demonstrate the denoising process, Figure 11 (a) and (b) shows both nonlinear enhancement of wavelet coefficients without and with denoising, respectively, for the input signal shown in Figure 10 (a). Figure 11 (c) shows the curve-fitting for threshold estimation.

2.1.6 Two dimensional extension

For image processing applications, the one dimensional structures discussed previously were simply extended to two dimensions. We adopted the method proposed by Mallat [26], shown in Figure 12, where filter $L(\omega) = \frac{1+|H(\omega)|^2}{2}$, and $H(\omega)$, $K(\omega)$ and $G(\omega)$ are the same filters used in the 1-D case.

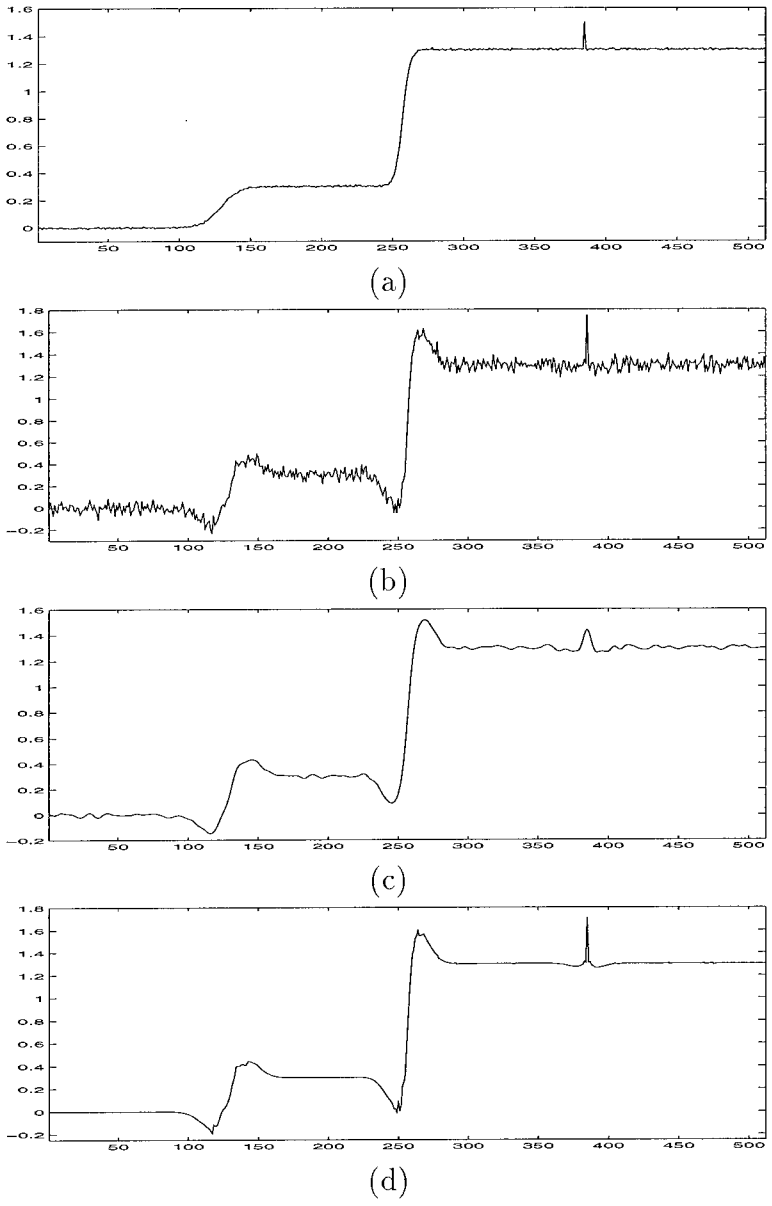

Figure 10: (a) Noisy input signal (contaminated by white Gaussian noise).
(b) Nonlinear enhancement without denoising, $G_m = 10$, $N = 4$, $t = 0.1$.
(c) Nonlinear enhancement of levels 2-3, $G_m = 10$, $t = 0.1$; levels 0-1 zeroed out;
(d) Nonlinear enhancement with adaptive wavelet shrinkage denoising, $G_m = 10$, $N = 4$, $t = 0.1$.

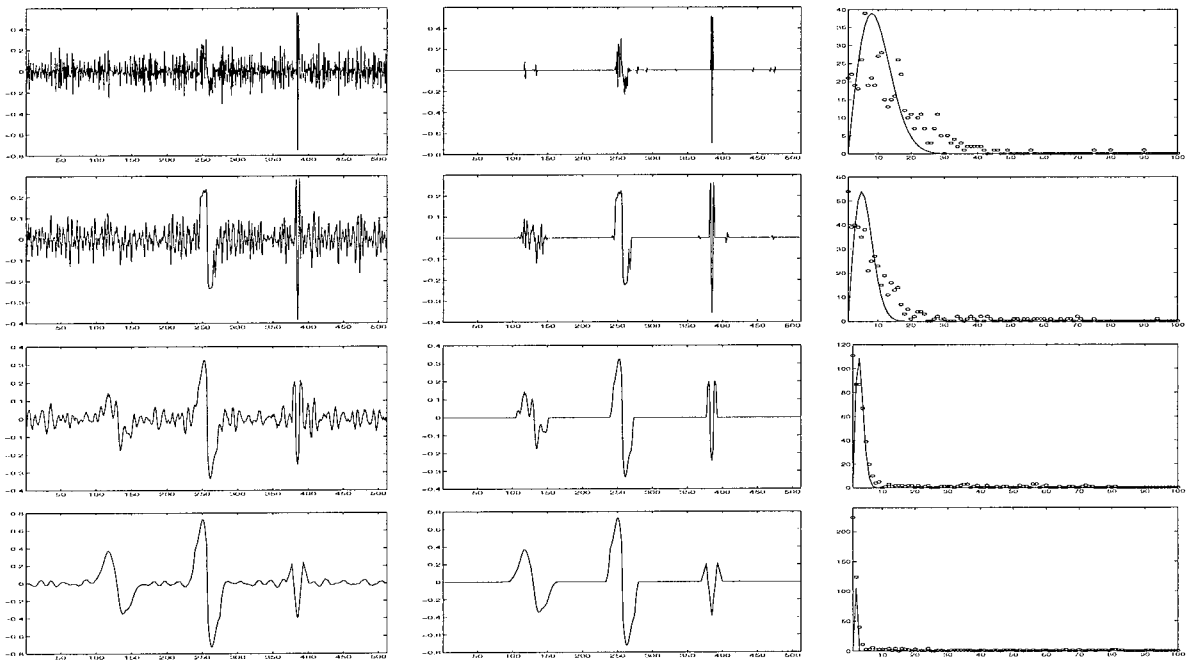

(a) (b) (c)

Figure 11: Column (a), Enhanced wavelet coefficients without denoising.
Column (b), Enhanced wavelet coefficients with adaptive thresholding $T_n = 4.5\eta$.
Column (c), The magnitude distribution and curve-fitting.
(Row 1 through 4 corresponds to levels 1 to 4.)

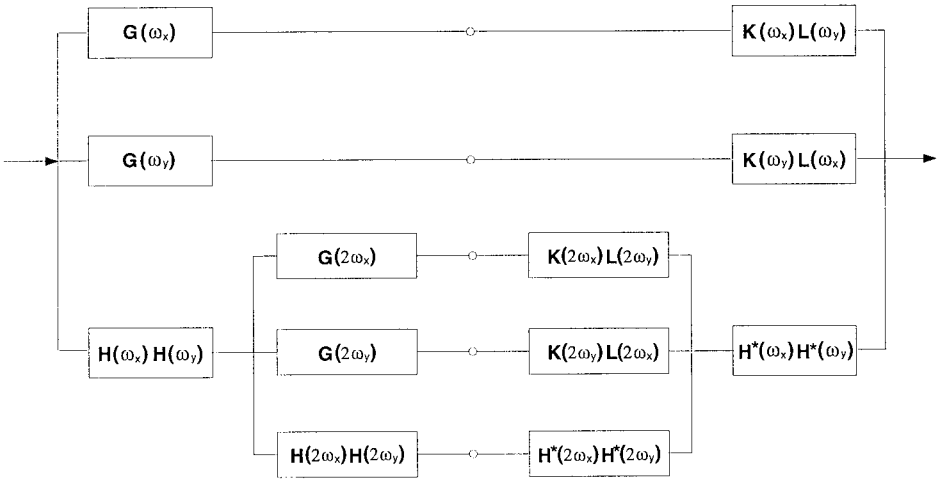

Figure 12: Two dimensional dyadic wavelet transform (two levels shown).

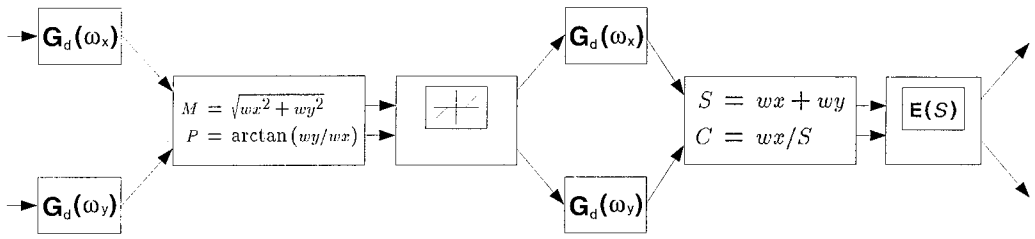

Figure 13: Denoising and enhancement for the 2-D case (level one shown).

However, experimental we observed that if we simply modify the two oriented wavelet coefficients independently, we introduced orientation distortions. One way to avoid this disastrous artifact is to apply a denoising operation on the magnitude of gradient coefficients, and apply a nonlinear enhancement operation on the sum of the Laplacian coefficients, as shown below in Figure 13. For the two oriented gradient coefficients wx_1 and wy_1, the magnitude M and phase P were computed as $M = \sqrt{wx_1^2 + wy_1^2}$ and $P = \arctan(wy_1/wx_1)$, respectively. The denoising operation was then applied to M, obtaining M'. The denoised coefficients were then simply restored as $wx_1' = M' * \cos(P)$ and $wy_1' = M' * \sin(P)$, respectively. For the enhancement operation, notice that the sum of two Laplacian components is *isotropic*. Therefore, we may compute the sum of the two Laplacian components $S = wx_2 + wy_2$ and $C = wx_2/S$. A nonlinear enhancement operator is then applied to only S, producing S'. Thus, the two restored components are $wx_2' = S' * C$ and $wy_2' = S' * (1 - C)$.

2.1.7 Experimental results and comparisons

In this section, we present sample experimental results and compare them with existing state-of-the-art techniques.

Figure 14 (a) shows a synthetic image with three circular "bumps" and added white noise. The enhancement results shown in (b) and (c) demonstrate unwanted noise amplification. Moreover, note that histogram equalization processing alters the object's boundary. However, the result shown in (d) accomplished by dyadic wavelet analysis produces a clearer image without orientation distortion.

Figure 15 (a) shows an original dense mammogram image with a central mass. The boundary of the mass in the the enhanced image was well defined and made clear penetration of spicules into the mass.

To study the efficacy of our algorithm, we blended mathematical phantom features into clinically proved cancer free mammograms. Figures 16 (a) and (b) show mathematical phantom features blended into M48 and M56 (resulting in Figure 17 (a) and Figure 18

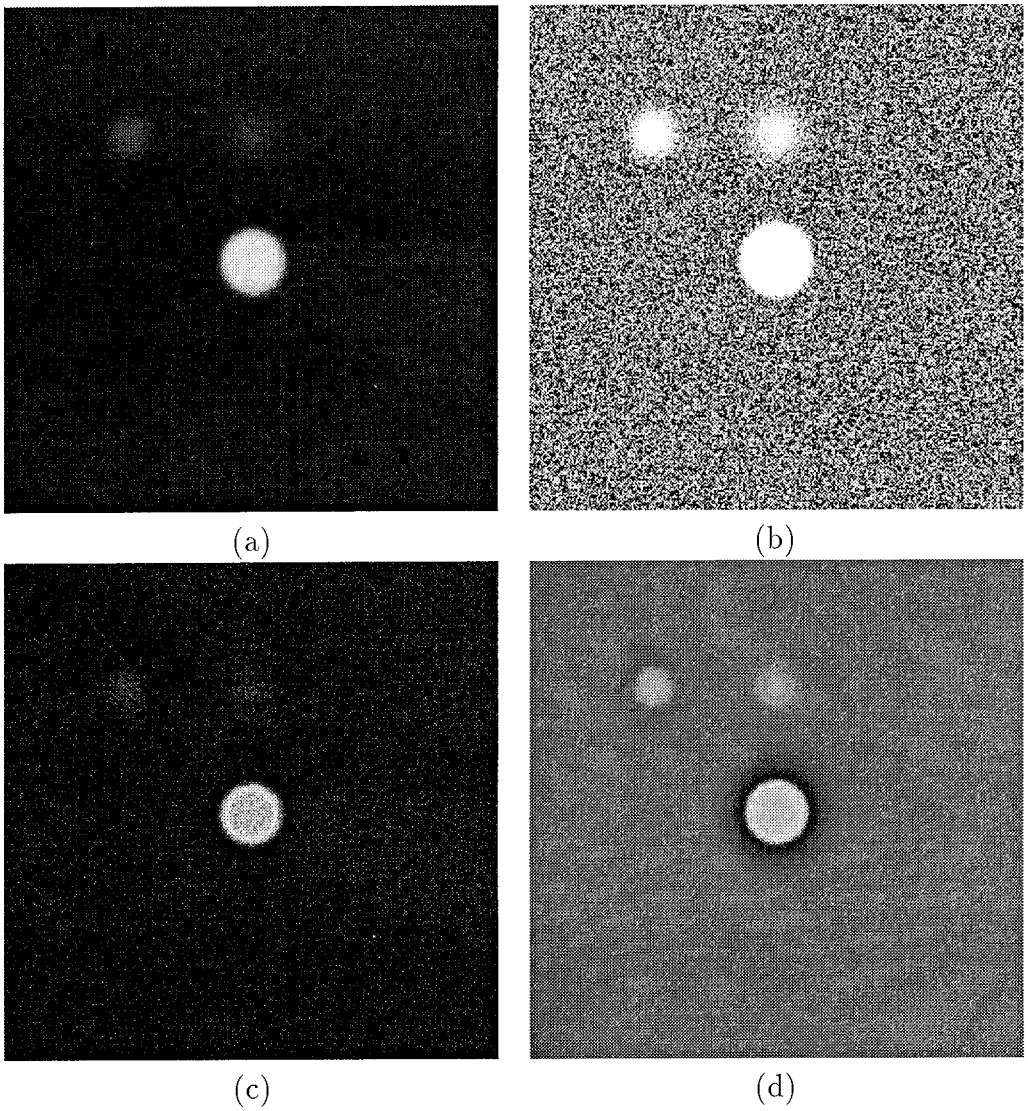

Figure 14: (a) Noisy image (white Gaussian noise contaminated).
(b) Histogram equalized. (c) Nonlinear enhancement by Beghdadi and Negrate's algorithm.
(d) Nonlinear enhancement with adaptive wavelet shrinkage denoising, $G_m = 20$, $N = 4$, $t = 0.1$.

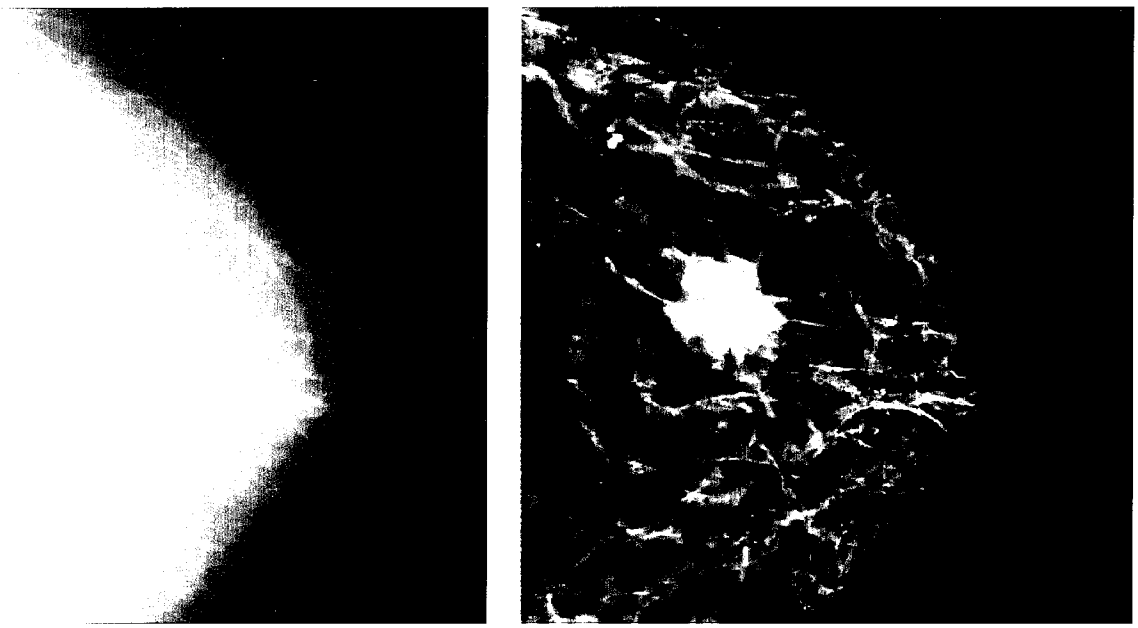

(a) (b)

Figure 15: (a) Oringinal mammogram image M73. (b) Nonlinear enhancement with adaptive wavelet shrinkage denoising. $G_m = 20$. $N = 5$. $t = 0.1$.

(a) (b)

Figure 16: (a) Phantom features blended into M48. (b) Phantom features blended into M56.

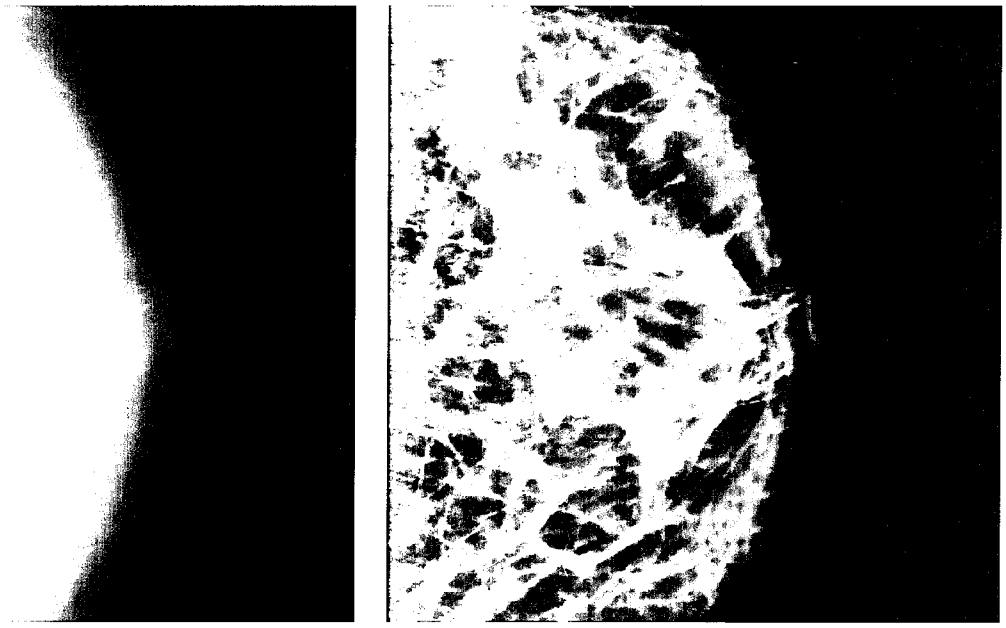

(a) (b)

Figure 17: (a) Mammogram image M48 with blended phantom features. (b) Nonlinear enhancement with adaptive wavelet shrinkage denoising. $G_m = 20$. $N = 5$. $t = 0.1$.

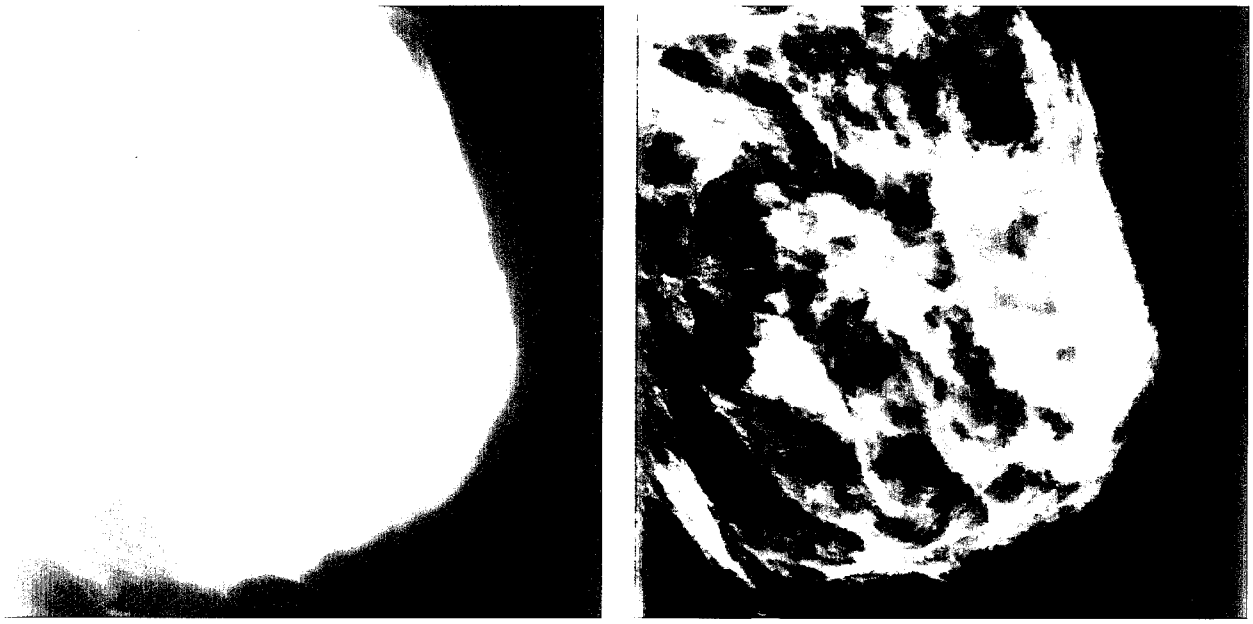

(a) (b)

Figure 18: (a) Mammogram image M56 with blended phantom features. (b) Nonlinear enhancement with adaptive wavelet shrinkage denoising. $G_m = 20$. $N = 5$. $t = 0.1$.

(a)), respectively.

Figure 17 (a) shows a dense mammogram with blended phantom features, and (b) shows an image processed by our nonlinear method. The enhanced image delineates well the boundary (uncompressed areas) of the breast and its structure. The phantom features were also well enhanced. Figure 18 (a) shows a dense mammogram with blended phantom features, and (b) shows the image enhanced.

2.1.8 Summary

We established connections between dyadic wavelet enhancement algorithms and traditional unsharp masking. We proved that two cases of linear enhancement were mathematically equivalent to traditional unsharp masking with Gaussian low-pass filtering. We designed a methodology for nonlinear enhancement with a simple nonlinear function to overcome the dynamic range requirement usually associated contrast enhancement of digital radiographs. By careful selection of wavelet filters and enhancement function, we showed that artifacts can be eliminated. An additional advantage of our simple enhancement function is that it includes traditional unsharp masking as a subset. We showed how an edge-preserved denoising stage (wavelet shrinkage) can be appropriately incorporated into our contrast enhancement framework, and introduced a method for adaptive threshold estimation. We showed how denoising and enhancement operations should be carried out for two dimensional images to avoid orientation distortions.

Our future research plan shall include the systematic study of gain and threshold parameters for the nonlinear enhancement. In addition, in the next year we shall seek localized and complex nonlinear methods to improve the performance of our existing algorithm.

2.2 XMam: An Image Editor for Mammography

2.2.1 Introduction

Recent estimates show that breast cancer is the most frequently diagnosed malignancy in the United States, accounting among women for 32% of all cancers detected and 18% of all cancer deaths [3]. Although mammography is widely recognized as the best method for the detection of breast cancer, 10%-30% of women who have breast cancer and undergo mammography have negative mammograms, and in approximately two-thirds of these false-negative mammograms the radiologist failed to identify cancers that were visible upon retrospective review of the radiographs [29]. In [30], Vyborny suggests that part of the problem resides in human search performance, a conclusion he bases on the following findings: (1) Lack of prior knowledge of the location of an abnormality decreases the likelihood that it will be detected, (2) In chest radiography, a large portion of the image is

not sampled by foveal vision during the radiologist's visual search, an effect that is also observed in mammography, although to a lesser extent because of the smaller size of the images, and (3) In searching for lung nodules, observers exhibit longer visual dwell times on a considerable portion of missed radiologic abnormalities than on normal areas, a phenomenon that is significant enough to allow for computer-based visual aids to reduce false-negative detections. Both [29] and [30] point out that replicated mammography readings (by two radiologists or a radiologists and a technologists) may increase selectivity and decrease the number of false-negative mammograms. One of the goals of computer-aided diagnostic schemes is to aid the radiologist in the search for lesions by indicating locations of suspicious abnormalities in mammograms.

When a suspicious region is detected, the radiologist must visually extract features from the finding and then either decide whether the abnormality is malignant or benign, or recommend additional screening, follow-up or biopsy. Although there are general guidelines to differentiate benign from malignant breast lesions, a considerable number of lesions are misclassified. For example, more than half of false-negative mammograms result from decisions by radiologists that the finding is either normal or benign [30], while only 10%-20% of masses in patients referred for surgical breast biopsy are malignant [29]. In [30], Vyborny suggests that part of the problem resides in the merging of multiple image features to characterize abnormalities. Although general radiologist can accurately and reproducibly extract individual image features of importance in mammography, they are usually outperformed by experienced mammographers in combining multiple features into a correct diagnosis [30]. One objective of computer-aided diagnostic schemes is to extract and analyze the characteristics of lesions to aid the radiologist in their classification.

Fundamental to the success of a computer-aided diagnostic methodology is the development of a large database of cases diagnosed as having signs of cancer based on mammographic screening, and later confirmed or denied as positive by biopsy. This database will serve as the ground truth for the development and verification of our computer algorithms for the detection of breast cancer. In this section of our report we describe the first version of a computer image editor that provides the necessary functionality to compile such database of cases.

2.2.2 Functionality

XMam is a software tool that allows radiologist to interactively indicate on digitized mammograms regions diagnosed as having signs of cancer. XMam's user interface has been designed to fit the needs of mammographic screening and consists of four image panels to allow for the simultaneous display of the craniocaudal (CC) and mediolateral oblique

(MLO) views of the left and right breasts (the four accepted views for breast cancer screening in the United States). As shown in Figure 19, XMam's interface is made up of two top windows which logically group the images corresponding to the CC and MLO views. These windows consist of left and right image panels equipped with vertical and horizontal scrollbars. The CC window is the application's main window and provides, in addition to its two image panels, three pull-down menus and one radio-box. In overview, XMam's functionality is supported by three logical modules: (1) an image module, (2) a data module and (3) a drawing module. In the next three sections we describe each of these modules in detail.

Image module

The image module manages image retrieval and display operations. This module provides a user with the necessary functionality for opening a patient's image file and displaying its contents in the corresponding windows. In the context of XMam, an image file refers to the logical grouping of the four standard radiographs obtained from a single mammographic screening. If for any reason, one or more images are missing from the patient's image file, the image module will leave blank the corresponding image panel(s).

A user may access the image module through the `Open` and `Close` buttons located in the `Image` pull-down menu on XMam's main window. The layout of this menu as well as other pull-down menus is shown in Figure 20. A point-and-click operation on the `Open` button of the `Image` pull-down menu pops up a `File Image Dialog` as the one shown in Figure 21, and allows a user to retrieve a patient's image file from the group of patients listed in its directory. A user may close a patient's image file either by opening a new file from the `File Image Dialog` or with a point-and-click operation on the `Close` button of the `Image` pull-down menu.

Data module

This module manages data update and retrieval operations. It provides a user with the necessary functionality for loading and saving a complex data structure that indicates which image regions were registered by a radiologist as having signs of cancer. A complete description of this data structure is described in detail below.

A user may access the data module through the `Load` and `Save` buttons located in the `Data` pull-down menu on XMam's main window. A point-and-click operation on the `Load` button of the `Data` pull-down menu pops up a `Load Dialog`, as shown in Figure 22(a), and allows a user to retrieve a patient's data structure. Similarly, a point-and-click operation on the `Save` button of the `Data` pull-down menu pops up a `Save Dialog` as shown in

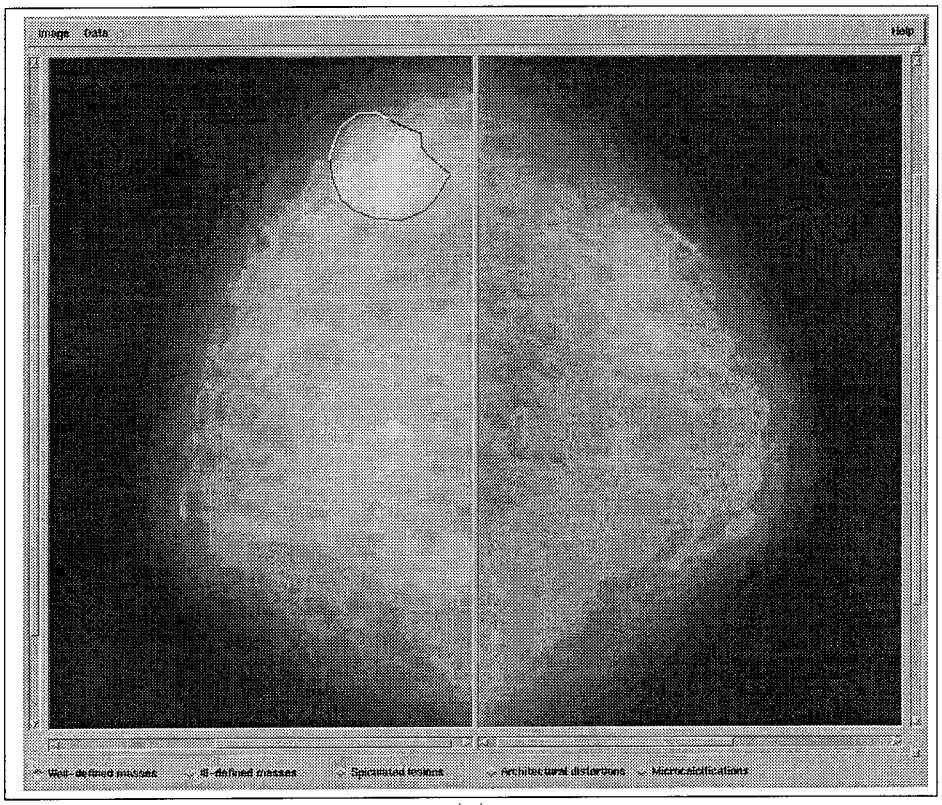

(a)

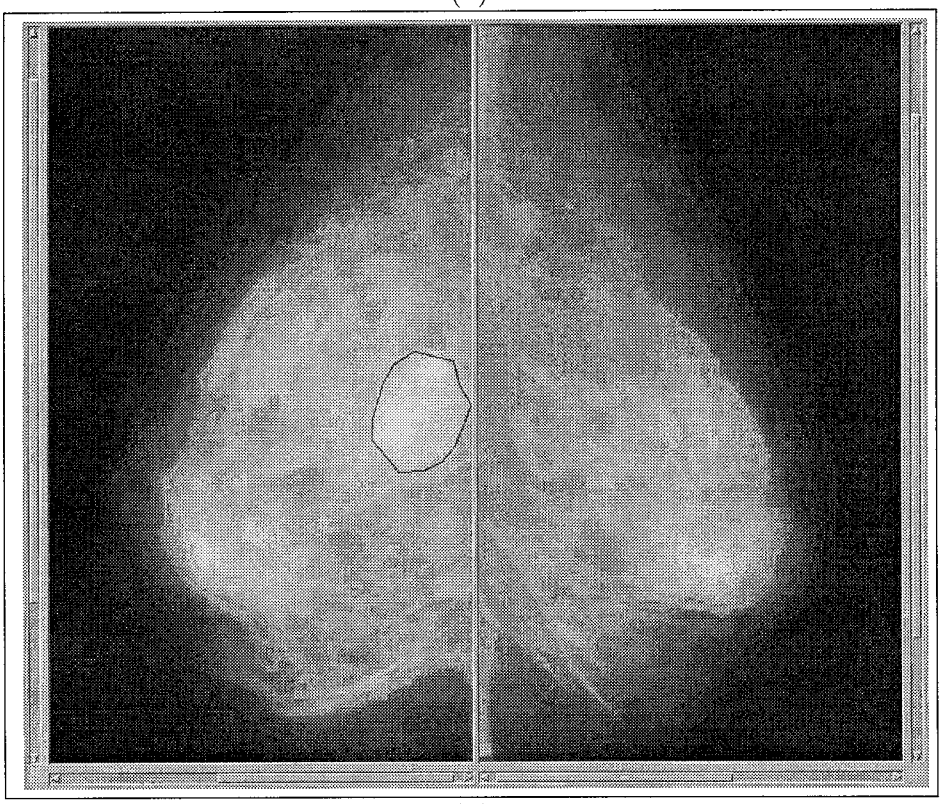

(b)

Figure 19: XMam's user interface: (a) CC window, (b) MLO window.

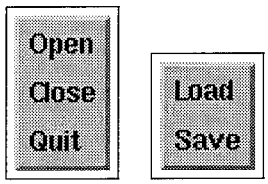

(a) (b)

Figure 20: XMam's pull-down menus: (a) Image menu, (b) Data menu.

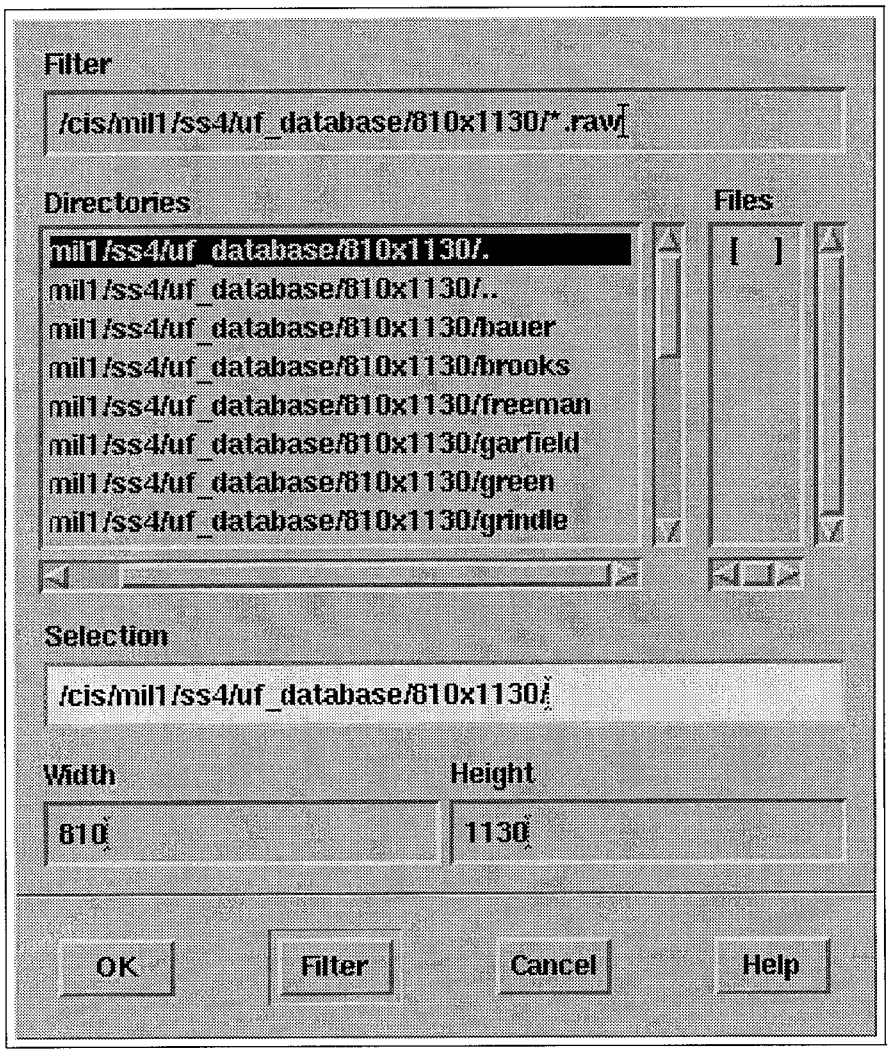

Figure 21: XMam's File Image Dialog.

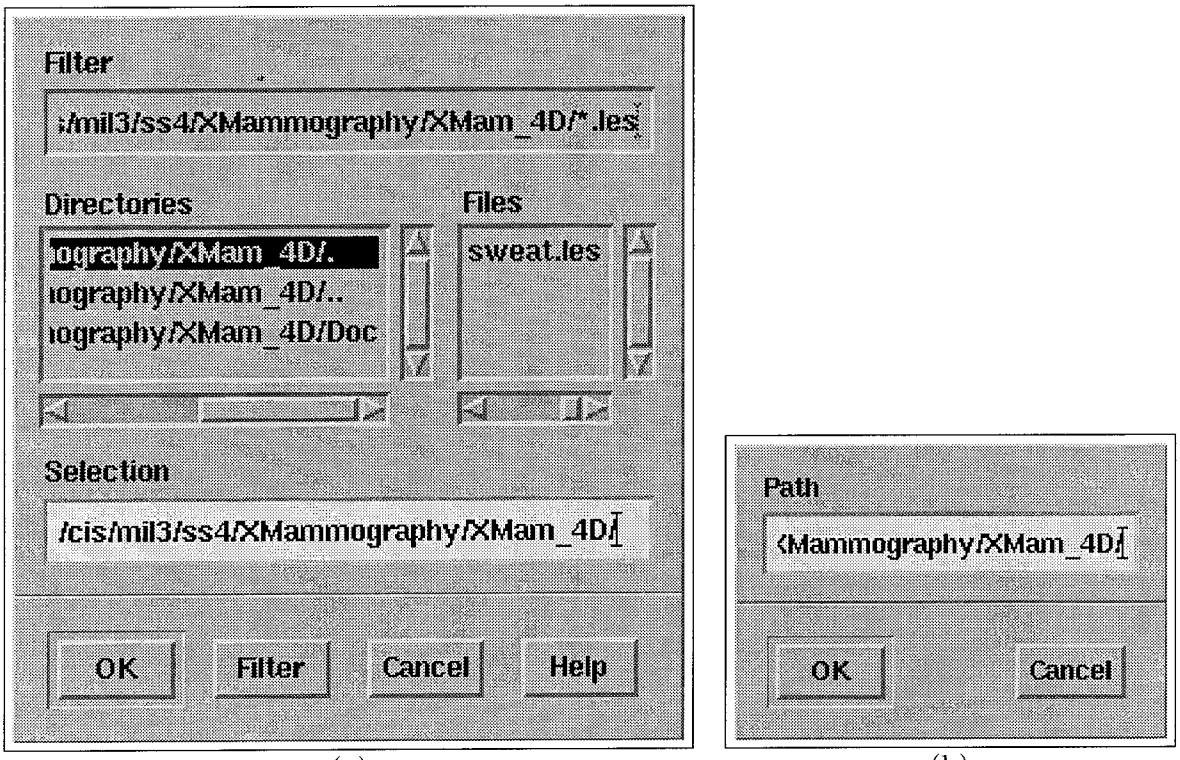

(a) (b)

Figure 22: XMam's File Data Dialogs: (a) Load Dialog, (b) Save Dialog.

Figure 22(b), and allows a user to store the data structure that contains the specific regions indicated by a radiologist as having signs of cancer.

Drawing module

The drawing module manages the drawing operations of XMam. This module provides a user with the necessary functionality for outlining image regions. This is accomplished with the aid of a computer mouse by enclosing regions of interest with polygons.

Before describing in detail XMam's drawing operations, we introduce some terminology that will simplify our discussion. In XMam, an active polygon group refers to a group of polygons on which a user is performing drawing operations. At any point in time there can be at most one such group. In general, a polygon group becomes active when a user performs a point-and-click operation on any of its polygons. A polygon that is being drawn is considered as active and forms a polygon group on its own. Polygon groups with more than one polygon are constructed by selecting several polygons and grouping them together by a group operation. A polygon group can be viewed conceptually as an unordered tuple of elements. Tuple elements may be single polygons or tuples themselves. This tuple feature allows a user to impose a complex logical structure into a polygon group. As an

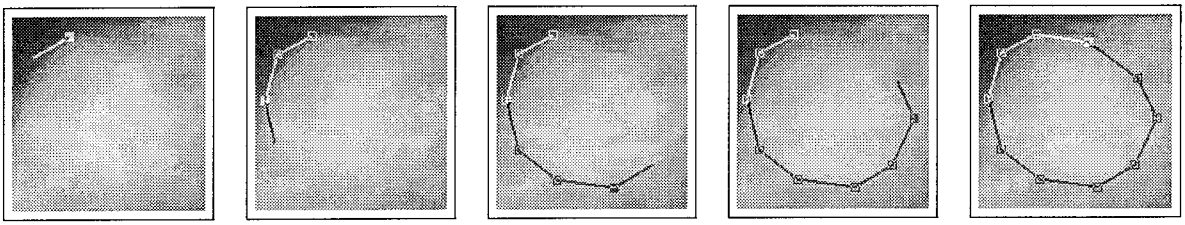

Figure 23: Outlining of a region of interest on XMam.

example, suppose that a and b are two polygons enclosing regions of interests corresponding to a single lesion visible on a given mammographic view, say the left craniocaudal (LCC). Then, a and b can be grouped together on a single tuple (a, b) to indicate that they are logically related. Also, suppose that c is a polygon enclosing a region related to the same lesion but visible on the complementary left mediolateral view (LMLO). To complete the lesion's description, polygon c should be grouped with tuple (a, b) to yield a complex group $((a, b), c)$. An important advantage of this tuple structure is that image regions that belong to the same lesion but that are visible on different views can be logically grouped together. Notice that this information may be useful for algorithms that rely on the simultaneous fusion of all four views for the detection of breast cancer. Another advantage of having polygon groups is that when a user selects any polygon, all other polygons that form part of its group become active. This provides immediate feedback as to which image regions are logically related. In addition this functionality can later be used for training new mammographers and technicians with previously diagnosed cases of breast cancer.

There are several drawing operations a user may engage at any given point in time. The simplest operation is that of drawing a polygon. Figure 23 shows several of the steps followed by a user to enclose a suspicious mass on a digitized mammogram. Recall that a polygon that is being drawn is considered an active polygon group, a state that is denoted in XMam by highlighting the vertices of the active polygons with square anchors. Figure 23 also shows that there are two classes of anchors in XMam, *active* and *inactive*. An active anchor is displayed as a solid square and denotes a polygon vertex on which the user may perform drawing operations. On the other hand, an inactive anchor is displayed as a clear square and cannot be operated on until it is in the active state. At any point in time there can be at most one active anchor within a polygon group. An anchor becomes active when a user performs a point-and-click operation on it. When an anchor is active, a user may adjust the anchor position, delete the anchor, or adjust the polygon position.

XMam provides four different mouse cursors to indicate its current state. We will refer to these cursors as crosshair, arrow, dotbox, and fleur. A crosshair cursor indicates that a user may start drawing a polygon at a given mouse position. If a user places the mouse

cursor on top of any line segment of an inactive polygon, the cursor will change from a drawing cursor to an arrow cursor to indicate that the user may select the inactive polygon by a point-and-click operation. Similarly, if a user places the mouse cursor on top of any line segment of an active polygon, the cursor will change from a drawing cursor to a dotbox cursor to indicate that the user may add an additional anchor to the polygon at the current mouse position. Also, if a user places the mouse cursor on top of any vertex of an active polygon, the mouse cursor will change from a drawing cursor to a fleur cursor to indicate that the user may adjust the anchor or polygon position by a point-and-click operation. The operation to be performed depends on which mouse button is pressed during the point-and-click operation. Adjustment of the anchor or polygon position may be carried out until the user releases the mouse button. In addition, a user may delete an active anchor by depressing the delete key.

Recall that there can be at most one active polygon group at any given time. We also mentioned that a polygon group with more than one polygon can be constructed by selecting several polygons and performing a group operation. Selecting a polygon makes it active, therefore we needed a special operation to override the constraint that *at most one polygon group* may be active at any point in time. This is accomplished in XMam by depressing the shift key. Polygon groups selected while depressing the shift key become active and can be grouped together by a group operation. If the group operation is not performed and the shift key is released, then selecting a new polygon will make it active and all other polygons inactive.

XMam not only allows a user to select regions of interests but also provides the functionality to classify them under five distinct lesion classes: (1) well-defined masses, (2) ill-defined masses, (3) spiculated lesions, (4) architectural distortions and (5) microcalcifications. Figure 24 shows a radio-box containing five radio-buttons, each associated with a distinct lesion class. Through this menu, a user may define a class under which any polygons drawn on the image panels are to be classified and displayed. In other words, the lesion menu provides a window into the lesion space and allows the user to display only those polygons that are related to a given lesion type. In the current version of XMam, a user is only allowed to display at any given time polygons belonging to a single lesion type. This limitation was imposed by our existing Sun workstation with 8-bit frame-buffers. Although there exist several software solutions for the problem, our solution is a hardware upgrade to a 24-bit frame-buffer. A temporary software solution was not implemented because we anticipate to port XMam to a 24-bit frame-buffer platform in the near future and determined that clouting (patching) the software with a partial solution would be detrimental to the real-time performance of the tool.

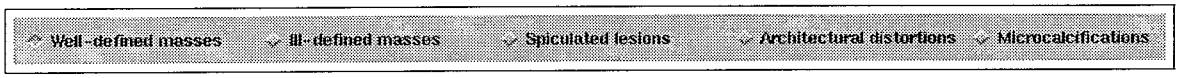

Figure 24: XMam's lesion menu.

2.2.3 Data structure

This section describes the data structures used by XMam to support drawing and grouping operations. As discussed above, a polygon group can be viewed as an unordered tuple of elements, where tuple elements may be single polygons or tuples themselves. In order to support this recursive structure, XMam represents a tuple by a linked list of cells, where cells may point to single polygons or other linked lists. Cells that point to single polygons are refered to as polygon cells, whereas cells that point to other linked lists are refered to as group cells. Figure 25 shows an instance of each of these two cell types with their corresponding data fields (the field used to identify the cell type was omitted for simplicity.) For any given cell c, `PPrevCell` and `PNextCell` are pointers to the cells preceding and succeeding c. For a polygon cell p, `PArray` serves as a pointer to an array that sequentially lists the `X` and `Y` coordinates of the polygon associated with p, `Panel` indicates the panel in which p's polygon will be displayed (LCC,RCC,LMLO,RMLO), `TOL` indicates the type of lesion p's polygon belongs to (well-defined mass, ill-defined mass, etc.), `NPoints` indicates the number of vertices of p's polygon, and `FPoint` indicates the index (if any) of the active anchor in p's polygon. For a group cell g, `PGFirst` and `PGLast` are pointers to the first and last cells, respectively, of the linked list associated with g's group. By including the `Panel` and `TOL` fields on each polygon cell we may create polygon groups consisting of polygons from different panels and having different lesion types. Although our current user interface only allows a user to form groups within a specific lesion type, our data structure already supports grouping across different lesion types. This additional grouping feature is provided in view of our plan to port XMam to a 24-bit framebuffer platform and use colors to indicate the lesion type of a polygon.

To keep track of all polygon groups, XMam compiles them into a single linked list. This list is accessed through a handle consisting of two fields, `PFirst` and `PLast`, that serve as pointers to the first and last cells of the list, respectively. In Figure 26 we show how the list handle, the polygon cells and the group cells are used together to represent the polygon group $((a, b), c)$ described in the previous section. We will refer to this complex data structure as the *region structure*. A more complex example consisting of two polygon groups, (a, b, c) and $((d, e), (f, g))$, is shown in Figure 27.

The region structure can be easily traversed by following the `PNextCell` pointers of its linked list. Every time a group cell is found, it is recursively expanded and its underlying

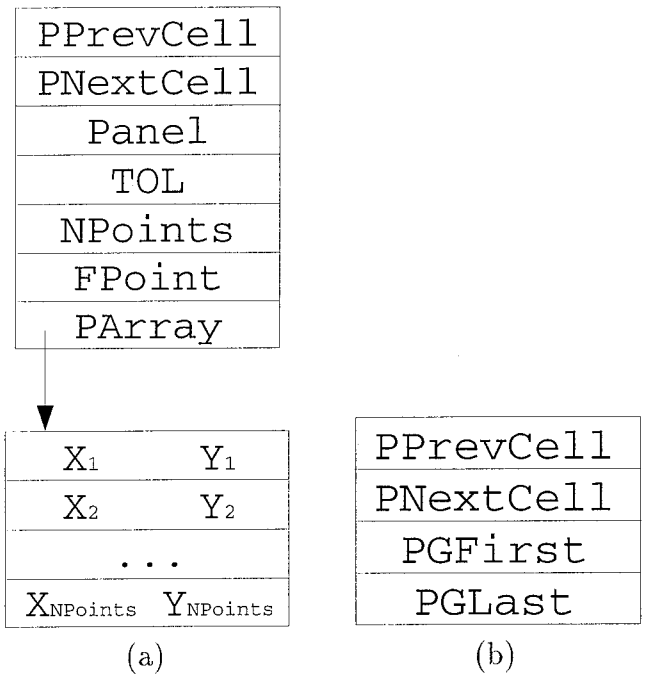

Figure 25: (a) Polygon Cell, (b) Group Cell.

list traversed. An example of this operation occurs when a user changes the type of lesion to be displayed and XMam traverses its region structure, clearing the polygons belonging to the previous lesion type and drawing the polygons corresponding to the new lesion type.

In addition to the region structure, XMam uses an auxiliary structure called the group structure to keep track of the active polygon group. Figure 28 shows an instance of the group structure consisting of a list handle and four list cells. The `LFirst` and `LLast` fields serve as pointers to the first and last cells of the list, respectively. Each list cell in turn points to a polygon group selected by a user. This list usually consists of a single entry pointing to the active polygon group but may contain several entries when a user selects several polygon groups for a grouping operation. The other three fields in the list handle function as different levels of addressing for the polygon that contains the active anchor. The `LCurr` field points to the list cell that points to the polygon group that contains the polygon cell with the active anchor. The `PGCell` field points to the group that directly contains the polygon cell with the active anchor. And the `PPCell` field directly points to the polygon cell that contains the active anchor. The reason for having these three distinct pointers is justified below.

We clearly require a pointer to the polygon cell with the active anchor to support possible edit, insert and delete operations. In addition, if a user deletes a polygon from a polygon group consisting of two polygons, then the group cell becomes unnecessary and needs to be deleted. The `PGCell` field provides efficient access to this cell. Similarly, if the

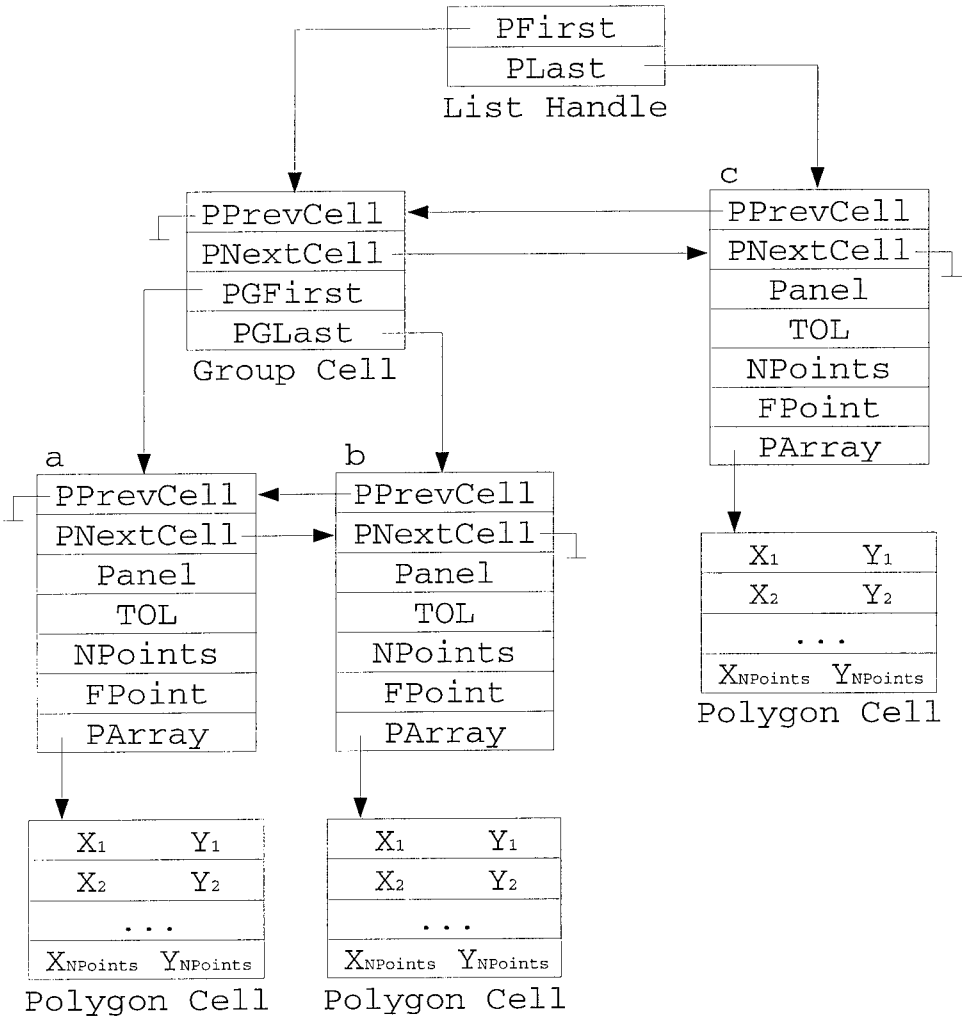

Figure 26: Structure for polygon group $((a, b), c)$.

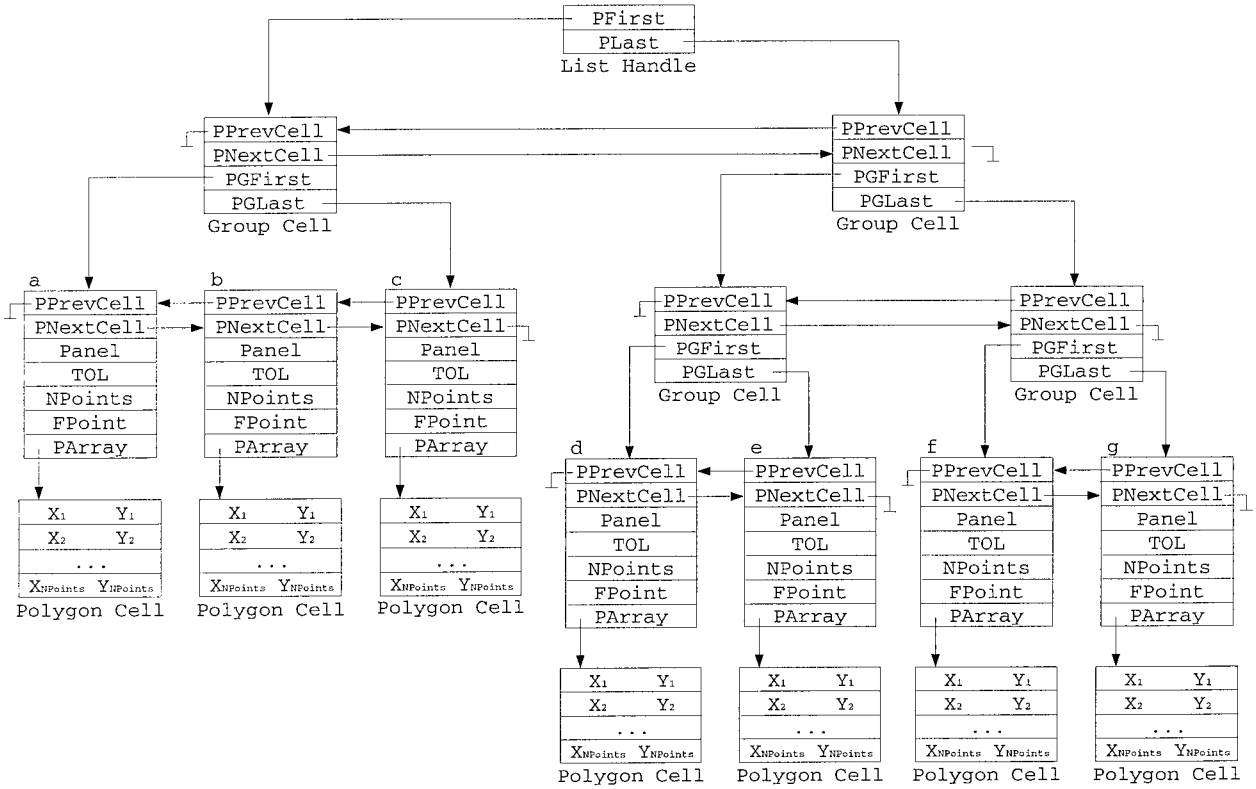

Figure 27: Structure for polygon groups (a, b, c) and $((d, e), (f, g))$.

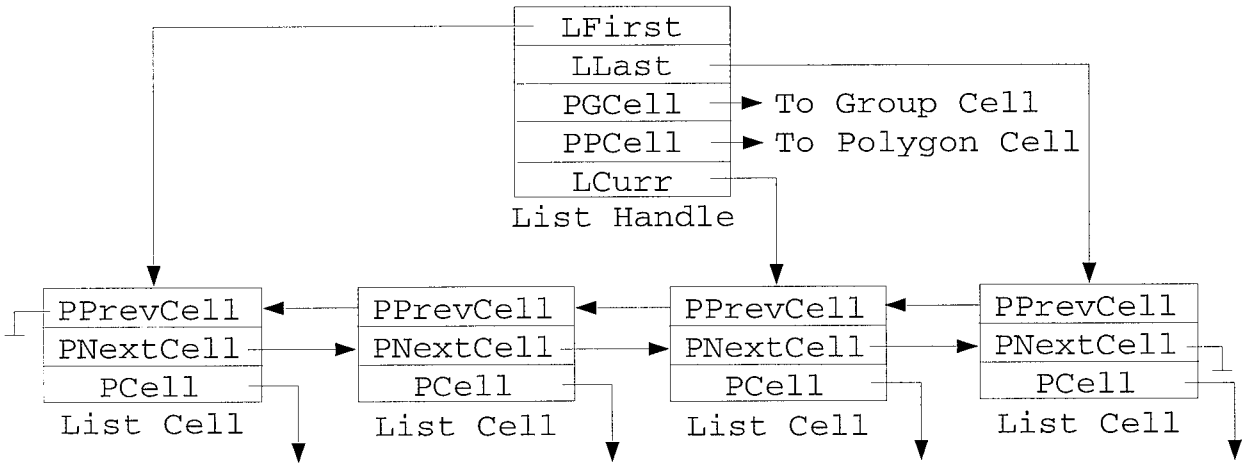

Figure 28: Group structure.

polygon group containing the active anchor consists of a single polygon and a user deletes this polygon, then the list cell becomes unnecessary and needs to be deleted. The `LCurr` field provides efficient access to this cell.

Although XMam uses several other data structures, the region and group structures described above comprise the major mechanisms used by XMam for managing drawing and grouping operations. Even though these data structures fully support the functionality described in the previous section, we anticipate that future versions of XMam shall yield cleaner and more efficient data structures.

2.2.4 Hardware

In this section we briefly describe our current hardware platform. The development environment for XMam is a dual-screen SPARCstation LX with 8-bit framebuffers, 64 Mbytes of memory and 320 MBytes of swap space. The platform currently runs Sun OS 4.1.3 and XWindows X11/R5, and includes the recently released Xvan server. This new server allows us to treat both screens as a single logical device and to freely move (drag) windows from one screen to the other.

2.2.5 Summary

We have described above the functionality and data structures of a computer image editor that can be used by radiologists to indicate on digitized mammograms regions diagnosed as probable cancer. This tool shall facilitate the compilation of a large database of diagnosed cases to be used as ground truth for the development and verification of our computer algorithms for the detection of breast cancer.

In the next year, XMam will progresively evolve into a state-of-the-art mammography workstation as new software is developed and hardware improvements are incorporated into our system.

2.3 Local Feature Analysis via Interval Wavelets

2.3.1 Introduction

This section of the report introduces a novel approach for accomplishing interactive feature analysis by overcomplete multiresolution representations. Traditional wavelets adapted to "life on an interval", can overcome "edge effects" of wavelet representations on a line. Methods of contrast enhancement are described based on two overcomplete multiresolution representations (interval wavelets): (1) Deslauriers-Dubuc interpolation, (2) Average interpolation.

We show quantitatively that transform coefficients, modified by an adaptive non-linear operator, can make more obvious unseen or barely seen features of mammography without requiring additional radiation.

Arbitrary regions of interest (ROI) of a mammogram are enhanced by average interpolation (AI) and Deslauriers-Dubuc interpolation (DD) representations on an interval. The results of local (ROI) enhancement and global enhancement of mammograms are compared quantitatively. We demonstrate that our method can provide radiologists with an interactive capability to support high-speed localized processing of selected (suspicious) areas (lesions).

We demonstrate that features extracted from multiscale representations can provide an adaptive mechanism for accomplishing local contrast enhancement. By improving the visualization of breast pathology we can improve chances of early detection while requiring less time to evaluate mammograms for most patients. In addition, we show that processing can be carried out at real-time (video frame) rates over selected areas of arbitrary shape. This is significant in consideration of the large image matrix size of digital mammograms.

2.3.2 Feature analysis via interval wavelets

In this section, we describe two multiresolution representations which were investigated: average interpolating wavelet transform [31], Deslauriers-Dubuc interpolation [32, 33]. These representations are attractive because they overcome the edge effect of traditional multiresolution representations (based on periodization of a finite signal to a signal on a line, or simply adding zeros to extend a signal on a line, etc). The shape of the basis functions for these representations are symmetric or antisymmetric, and allow for perfect reconstruction. We have used these representations to decompose an arbitrary rectangle of a mammogram, so that the rectangle may be analyzed independently.

Cohen and Daubechies [34] first adapted multiresolution analysis on the line to "life on the interval", where a sequence of successive approximation spaces on the interval were be constructed as: $\overline{\bigcup_{j\in\mathbf{Z}} V_j} = \mathbf{L}^2([0,1])$, $\bigcap_{j\in\mathbf{Z}} V_j = \{0\}$. By defining W_j as an orthogonal complement of V_j in V_{j-1}, $V_{j-1} = V_j \bigoplus W_j$, the space $\mathbf{L}^2([0,1])$ can be represented as a direct sum $\mathbf{L}^2([0,1]) = \bigoplus_{j\in\mathbf{Z}} W_j$.

In the following two representations, the bases are compactly supported, but not orthogonal. These representations are often called *overcomplete redundant representations.*

Deslauriers-Dubuc interpolation

This multiresolution representation consists of the Deslauriers-Dubuc fundamental functions [32, 33]. Suppose D is an odd integer and $D > 0$, a fundamental function can be

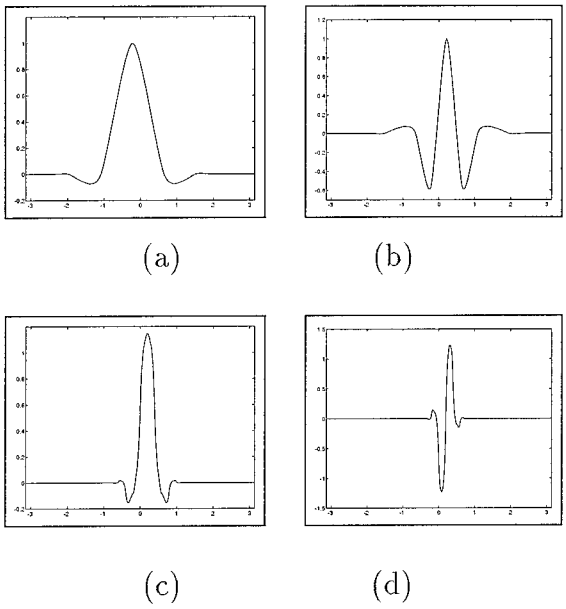

Figure 29: (a) Refinement relation for Deslauriers-Dubuc interpolation. (b) DD wavelet plot, $D = 3$. (c) Refinement relation for average interpolation. (d) AI wavelet plot,$D = 2$.

defined by interpolating the Kronecker sequence recursively: if F_D has been defined in the set of B_0 at dyadic rationals $k/2^0, k \in \mathbf{Z}$, then extend F_D to the set of $B_1, B_2, \ldots, B_j, j \in \mathbf{Z}$. Specifically, when the value of the function is defined at all the dyadic rationals $k/2^j, k \in \mathbf{Z}$, we extend the function by polynomial interpolation to all dyadic rationals at $k/2^{j+1}, k \in \mathbf{Z}$, this means extend the function to all the dyadic rationals half way between the previously defined positions. When $j \to \infty, F_D$ converges to a unique continuous function on the real line. This function defines an $(\mathbf{R}, D)$ interpolating wavelet for $\mathbf{R} = \mathbf{R}(D)$, and is compactly supported. Figure 29 shows the fundamental solution of DD interpolation and associated wavelets ($D = 3$).

Donoho [31] showed that given a $(\mathbf{R}, D)$ interpolating wavelet ψ, we can construct an interpolating wavelet transform, mapping the function f into approximation sequence $s_{j_0,k}$, and detail sequence $d_{j_0,k}, d_{j_0+1,k}, d_{j_0+2,k}, \cdots, d_{j_0+m,k}, m \in \mathbf{Z}, m \to \infty$. The function f can then be reconstructed from its coefficients,

$$f = \sum_k s_{j_0,k}\phi_{j_0,k} + \sum_{j \geq j_0} \sum_k d_{j,k}\psi_{j,k}.$$

By adapting the inhomogenous interpolating transform to "life on the interval", we can develop additional interpolating wavelet transforms for $\mathbf{C}[0,1]$. Suppose that $\phi_{j,k}$ is a scaling function on the line. The scaling functions on the interval $\psi_{j,k}^{interv}$ are derived in the following way: (1) in the interior of the interval, they are just the same as on the line

$$\phi_{j,k}^{interv} = \phi_{j,k}, \qquad D < k < 2^j - D - 1$$

(2) on the edges of the interval, they are dilations of boundary adjusted functions:

$$\phi_{j,k}^{interv} = 2^{j/2}\phi_k^{left}(2^j x - k), \qquad 0 \le k \le D,$$

$$\phi_{j,2^j-k-1}^{interv} = 2^{j/2}\phi_k^{right}(2^j x - 2^j - k - 1), \qquad 0 \le k \le D.$$

Thus for the spaces $V_j[0,1]$ we have the functions:

$$\phi_{j,k}^{interv} = \begin{cases} \phi_{j,k}^{left} & 0 \le k \le D \\ \phi_{j,k} & D < k < 2^j - D - 1 \\ \phi_{j,k}^{right} & 2^j - D - 1 \le k \le 2^j. \end{cases}$$

in the same way, we can define the wavelets on the interval for the detail spaces $W_j[0,1]$:

$$\psi_{j,k}^{interv} = \begin{cases} \psi_{j,k}^{left} & 0 \le k < \lfloor D/2 \rfloor \\ \psi_{j,k} & \lfloor D/2 \rfloor \le k < 2^j - \lfloor D/2 \rfloor \\ \psi_{j,k}^{right} & 2^j - \lfloor D/2 \rfloor \le k < 2^j. \end{cases}$$

Thus the function $f \in V_{j+1}[0,1]$ can be written as

$$f = \sum_{k=0}^{2^j-1} s_{j,k}\phi_{j,k}^{interv} + \sum_{k=0}^{2^j-1} d_{j,k}\psi_{j,k}^{interv}.$$

Average interpolating wavelet transform

Donoho [31] showed that connected with Deslauriers-Dubuc interpolation, there exists an *average interpolating wavelet transform.* Let D be an even integer and $D > 0$, starting from the Kronecker sequence $a_{0,k} = \delta_{k,0}$, $k \in \mathbf{Z}$, we synthesize the averages $(a_{j,k})_k, j \in \mathbf{Z}+$, the sequence $A_{j,D} = \sum_k a_{j,k} 1_{[k/2^j,(k+1)/2^j]}(t)$ shall converge uniformly to a fundamental solution of the interpolating scheme A_D, and has compact support. Figure 30 shows the refinement relation and its associated wavelets with $D = 2, 4$.

$A(t)$ may be written as

$$A(t) = \sum_k a_{0,k} A_D(t-k).$$

Thus the average interpolating wavelet transform is closely related with Deslauriers-Dubuc interpolation. Let $D \ge 2$ be an even integer, and let $\phi = A_D$ be the fundamental solution of the average interpolation, and $\phi^{DD} = F_{D+1}$ (where "DD" represents *Deslauriers-Dubuc interpolation*) be a fundamental solution of the Deslauriers-Dubuc interpolation. Let ψ be the AI (where "AI" represents the *average interpolation*) wavelet, and let ψ^{DD} be the DD wavelet. Then there exists a relation:

$$\frac{d}{dx}\phi^{DD}(x) = \phi(x+1) - \phi(x)$$

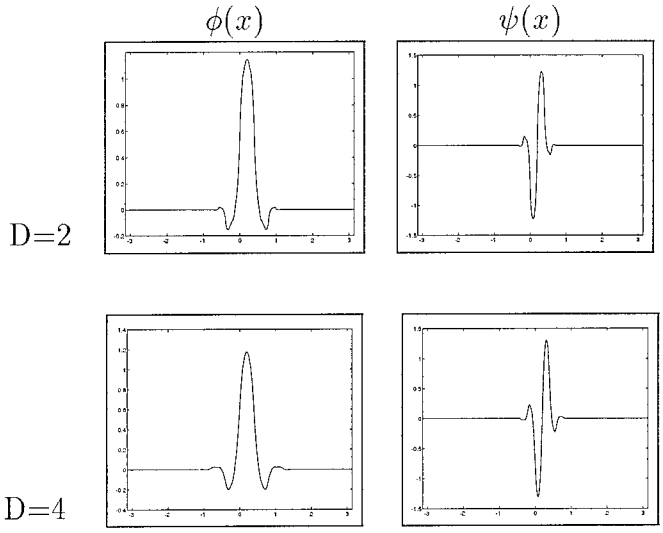

Figure 30: Scaling functions and associated AI wavelets.

$$\psi(x) = -\sqrt{2}\frac{d}{dx}\psi^{DD}(2(x-1/2))$$

as shown in Figure 29. If the ϕ and ψ are associated with the average interpolation, we can expand the function $f \in V_{j1}$ into a sequence of coefficients at coarse scale in the spaces $V_{J_0}, j_0 < j_1$, and a series of details:

$$f = \sum_k s_{j_0,k}\phi_{j_0,k} + \sum_{j_0<j<j_1}\sum_k d_{j,k}\psi_{j,k}.$$

By adapting the inhomogenous interpolating transform on an interval", interpolating wavelet transforms for $\mathbf{L}^1[0,1]$ can be constructed. For the spaces $V_j[0,1]$ we have the functions:

$$\phi_{j,k}^{interv} = \begin{cases} \phi_{j,k}^{left} & 0 \le k \le D \\ \phi_{j,k} & D < k < 2^j - D - 1 \\ \phi_{j,k}^{right} & 2^j - D - 1 \le k \le 2^j. \end{cases}$$

in the same way, we can define the wavelets on the interval for the detail spaces $W_j[0,1]$:

$$\psi_{j,k}^{interv} = \begin{cases} \psi_{j,k}^{left} & 0 \le k < D/2 \\ \psi_{j,k} & D/2 \le k < 2^j - D/2 \\ \psi_{j,k}^{right} & 2^j - D/2 \le k < 2^j. \end{cases}$$

Thus the function $f \in V_{j+1}[0,1]$ can be written as

$$f = \sum_{k=0}^{2^j-1} s_{j,k}\phi_{j,k}^{interv} + \sum_{k=0}^{2^j-1} d_{j,k}\psi_{j,k}^{interv}.$$

Figure 31 shows plots of an AI refinement relation and its associated wavelets on the interval.

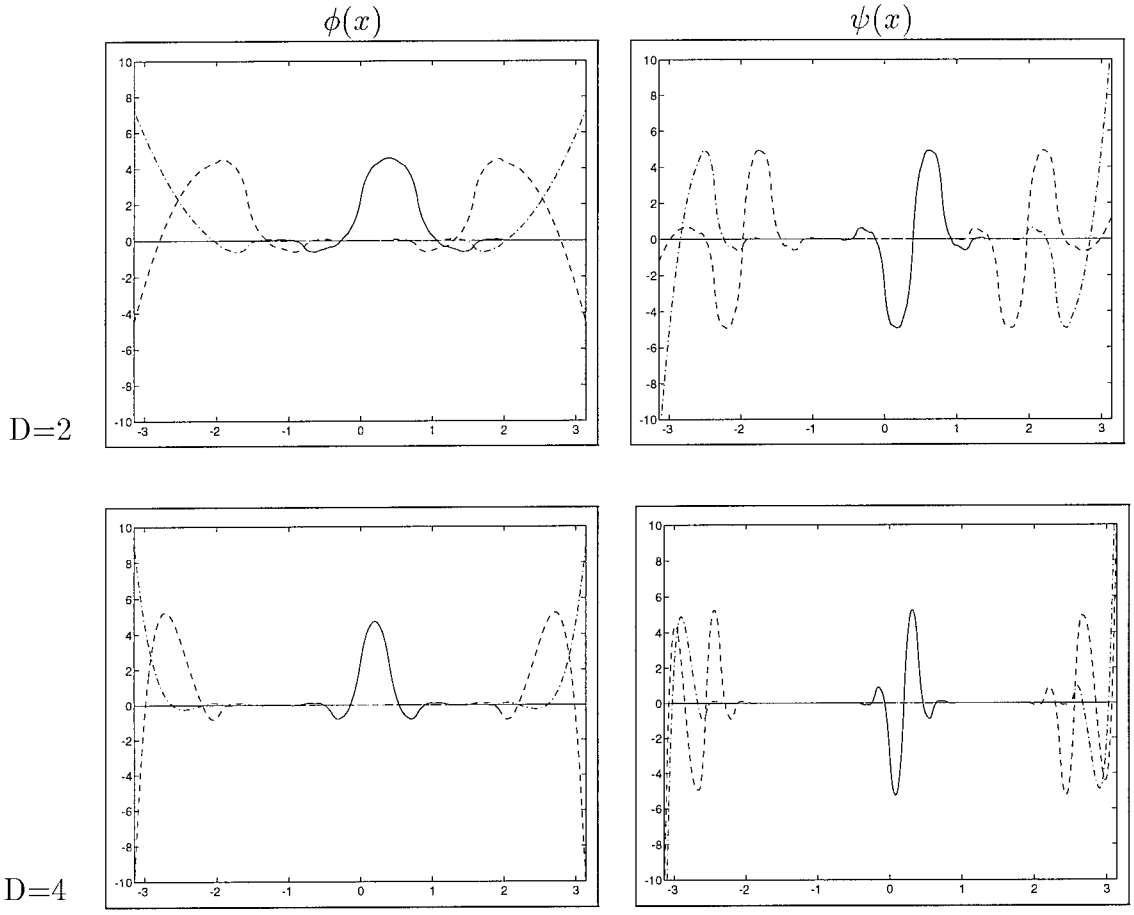

Legend:

——— Wavelets on the interior of interval.

— · —· Wavelets on the edges.

— — — Wavelets on the edges close to "heart" of interval.

Figure 31: AI wavelets and scaling functions on the interval $[0, 1]$.

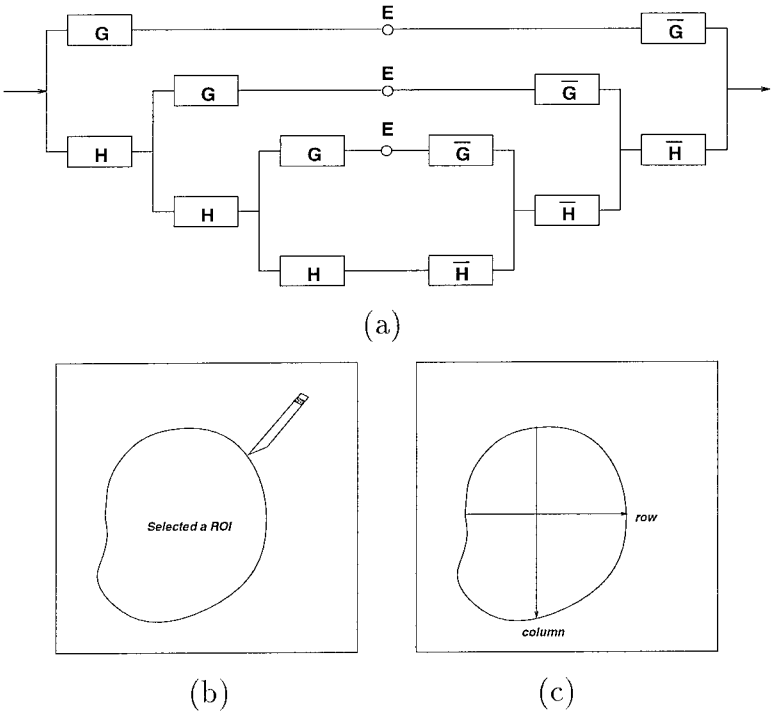

Figure 32: (a) Decomposition and enhancement tree structure for one dimensional case. H and G are a filter pairs. E is a nonlinear operator for enhancement. (b) Selected ROI within a mammogram, (c) ROI is processed based on tensor product: each row is processed first, followed by the processing of each column.

Implementation

Figure 32(a) shows the one dimensional case of a tree structure analysis filter bank, used to implement the above transformations. After decomposition of an original signal, enhancement (defined by E) is applied to wavelet coefficients. The enhanced signal is then obtained by reconstructing the signal from the modified coefficients. By extending the processing for the one dimensional case to two dimensions, we were able to enhance features of mammography by using the average interpolation and Deslauriers-Dubuc interpolation wavelet transforms. For processing of an arbitrary region in a mammogram, we used a scanline based method: First, the rows of a selected ROI were scanned and processed, then the columns. Figures 32(b) and (c) illustrates the processing steps graphically.

Enhancement techniques

To accomplish multiscale contrast enhancement, non-linear techniques for image enhancement are applied to the multiresolution representations. In our case, there are four components in the transform space: horizontal, vertical, diagonal, and DC component, represented by h^i, v^i, d^i, c^i respectively, where i is the level of a transform. Let x be the original mammogram, f be the function designed to emphasize features of importance within a selected level i, L be the total level of transform. Then the enhanced image may be given by

$$\hat{x} = \sum_{i=1}^{L} W^{-1}(f(h^i), f(v^i), f(d^i), c^i). \tag{17}$$

In general, by defining function g, we can denote specific enhancement schemes for modifying the coefficients within distinct levels of scale-space.

There are three ways of enhancement techniques: local enhancement technique based on multiscale edges, global enhancement techniques of multiscale histogram equalization and multiscale adaptive gain processing

Experimental results and discussion

Preliminary results have shown that the multiscale processing techniques described above can make more obvious unseen or barely seen features of a mammogram without requiring additional radiation. Our study suggests that the analyzing functions presented in this paper can improve the visualization of features of importance to mammography and assist the radiologist in the early detection of breast cancer.

Figure 33(a) shows a "dense" mammogram. This class of mammogram is more typical in younger females due to the greater absorption of X-ray energy by less fatty tissues in the breast. They remain particularly difficult to diagnose due to lack of contrast, even for

radiologists specializing in mammography. Figure 33(c) shows the result of global wavelet processing for four levels of analysis. In this case, the values of transform coefficients within each level of a decomposition (excluding the DC cap) were modified by histogram equalization independently. Since the coefficients are space-frequency representations, contrast modifications on the transform side are preserved in part on the spatial side. Similar contrast gains were observed for additional dense radiographs. Figure 33(b) displays the result of standard histogram equalization. Unfortunately, the dense tissues of the breast image are "washed out" in Figure 33(b).

Mathematical models of phantoms were constructed to validate our enhancement techniques against false positives arising from possible artifacts introduced by the analyzing functions and to compare our methods against traditional image processing techniques of improving contrast. Our models included features of regular and irregular shapes and sizes of interest in mammographic imaging, such as microcalcifications, cylindrical and spicular objects, and conventional masses. Techniques for blending a normal mammogram with the images of mathematical models were developed. The purpose of these experiments was to test the *performance* of our processing techniques on inputs known a priori using mammograms where the objects of interest were deliberately obscured by normal breast tissues. The imaging justification for blending is readily apparent; a cancer is visible in a mammogram because of its (slightly) higher X-ray attenuation which causes a lower radiation exposure on the film in the appropriate region of a projected image.

Figure 34(b) shows an example of a mammogram whereby the mathematical phantom shown in Figure 34(c) has been blended into a clinically-proven, cancer-free mammogram. The blended image was shown in Figure 36(a), it was constructed by adding the amplitude of the mathematical phantom image in Figure 34(c) to the cancer free mammogram in Figure 34(b) followed by local smoothing of the combined image.

Radiologists at Shands Hospital at the University of Florida validated that processing the blended mammogram with our local enhancement techniques introduced no significant artifacts and preserved the shapes of the known mammographic features (calcifications, dominant masses, and spicular lesions) contained in the original mathematical phantom.

A quantitative measure of contrast improvement can be defined by a Contrast Improvement Index (CII),

$$\mathrm{CII} = \frac{C_{\mathrm{Processed}}}{C_{\mathrm{Original}}},$$

where $C_{\mathrm{Processed}}$ and C_{Original} are the contrasts for a region of interest in the processed and original images, respectively.

In this study we adopt a version of the optical definition of contrast introduced by

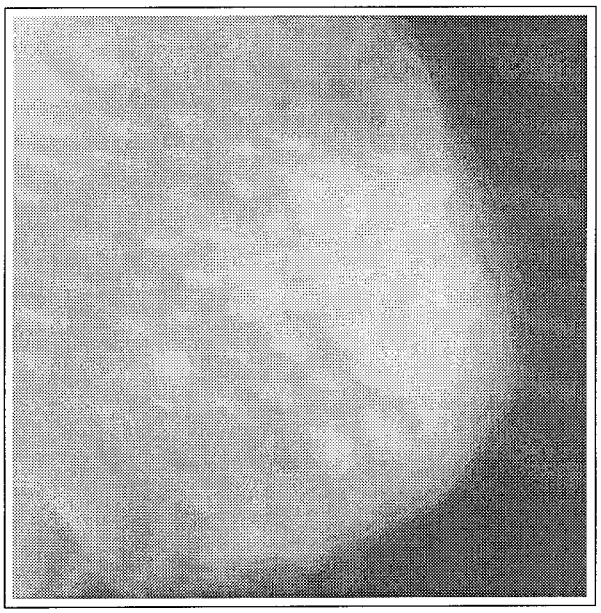

(a)

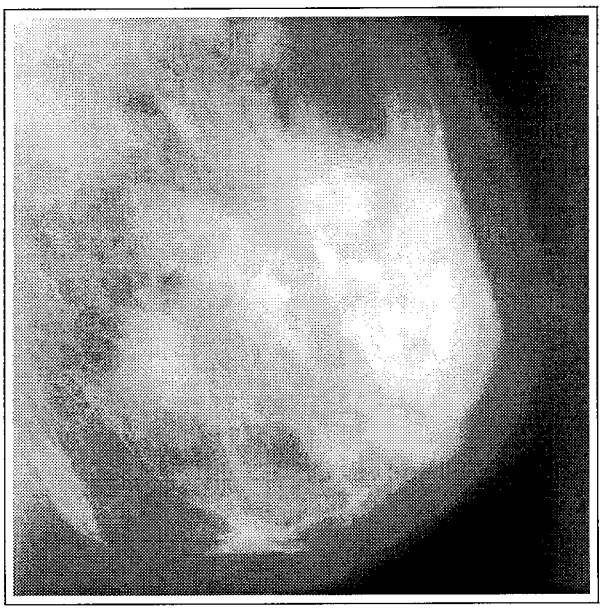

(b)

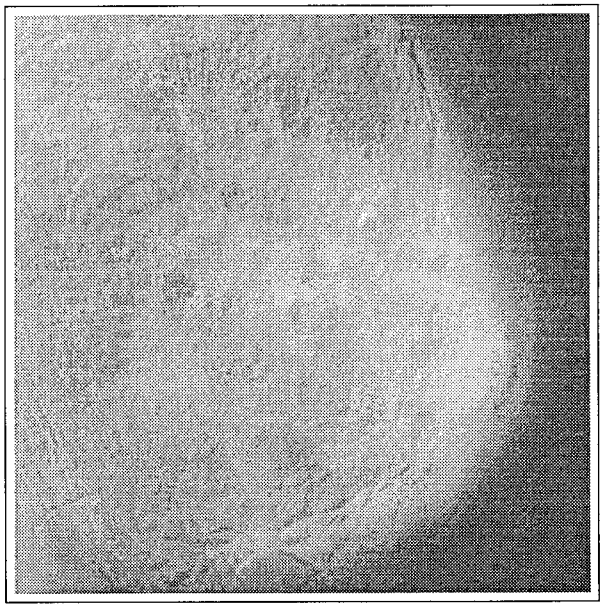

(c)

Figure 33: (a) Original dense mammogram, M56. (b) Enhancement by traditional histogram equalization. (c) Global enhancement by adaptive histogram equalization of Deslauriers-Dubuc interpolation (DD).

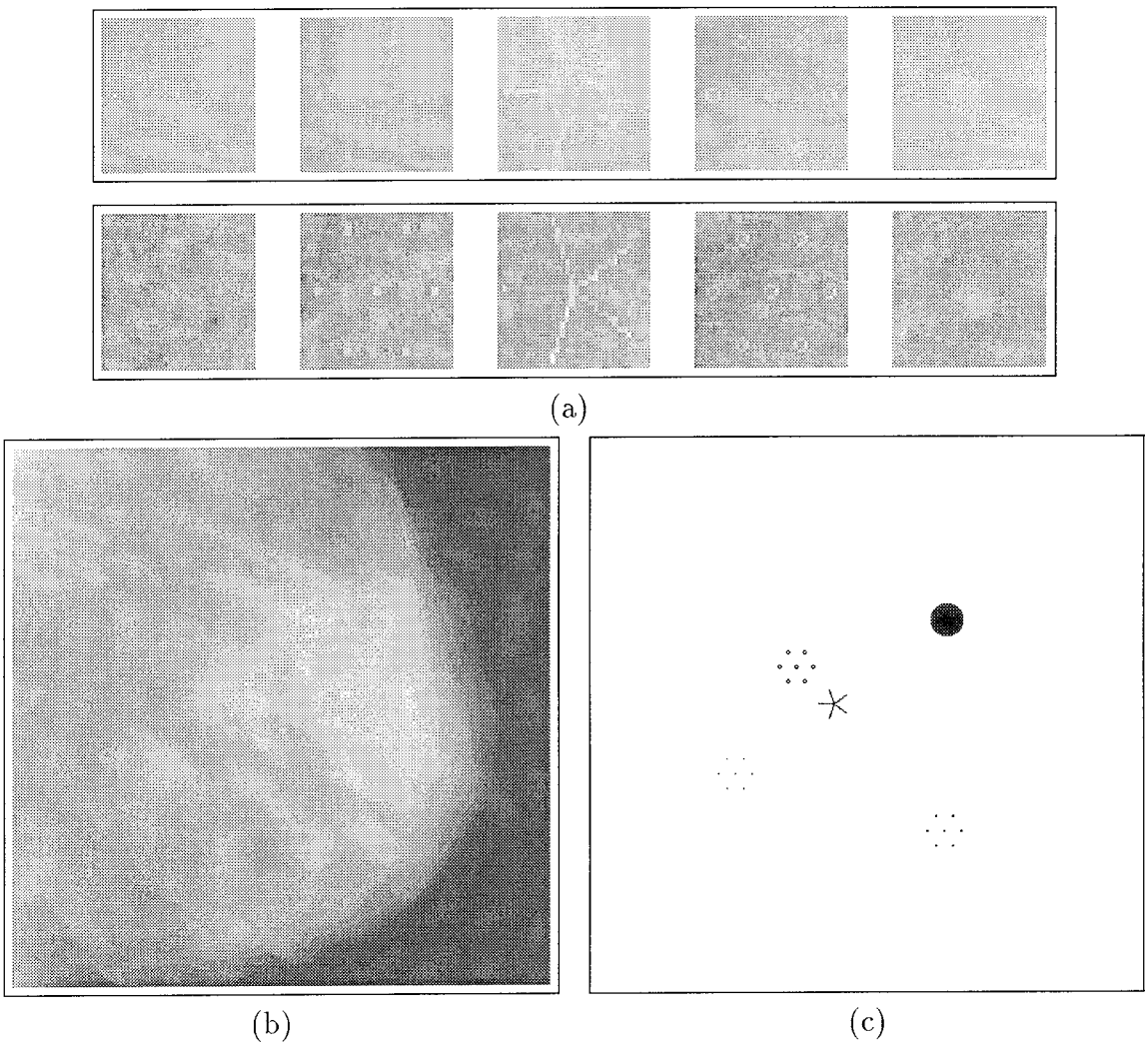

Figure 34: (a) Contrast enhancement by adaptive gain processing of DD interpolation wavelets. (b) Original dense mammogram, M56. (c) Mathematical phantom.

Table 1: Contrast values for enhancement by local enhancement by multiscale edges obtained from average interpolation (AI), Deslauriers-Dubuc interpolation (DD).

Contrast values for local enhancement techniques			
Feature	C_{Original}	C_{AI}	C_{DD}
Minute microcalcification cluster	0.0498	0.1697	0.1833
Microcalcification cluster	0.0324	0.0733	0.1040
Spicular lesions	0.0272	0.0728	0.0836
Circular (arterial) calcification	0.0378	0.1060	0.1242
Well-circumscribed mass	0.0032	0.0046	0.0051

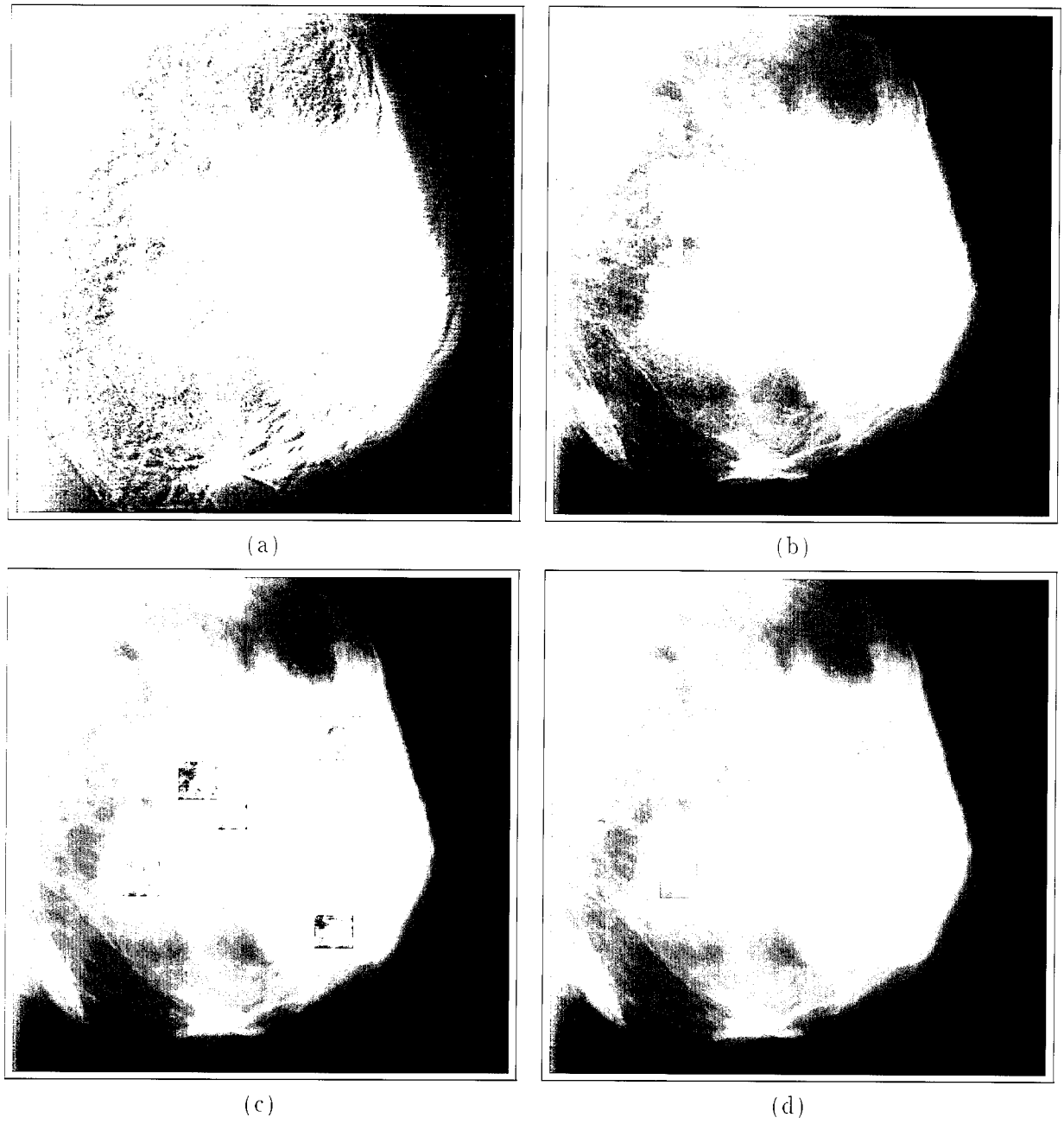

Figure 35: Blended mammogram: (a) Global enhancement by DD gain. (b) Local enhancement by DD edges. (c) Enhancement of rectangular regions by DD gain. (d) Enhancement of rectangular regions by DD edge processing.

Table 2: CII for enhancement by local enhancement by multiscale edges obtained from average interpolation (AI),Deslauriers-Dubuc interpolation (DD).

Contrast Improvement Index (CII) for local enhancement techniques		
Feature	CII_{AI}	CII_{DD}
Minute microcalcification cluster	3.4051	3.6773
Microcalcification cluster	2.2605	3.2061
Spicular lesions	2.6756	3.0728
Circular (arterial) calcification	2.8012	3.2828
Well-circumscribed mass	1.4364	1.6024

Morrow et al [35]. The contrast C of an object is defined by

$$C = \frac{f - b}{f + b},$$

where f is the mean gray-level value of a particular object in the image, called the *foreground*, and b is the mean gray-level value of a surrounding region called the *background*. This definition of contrast has the advantage of being independent of the actual range of gray levels in the image. With the aid of the mathematical phantom we computed local masks to separate the foreground and background regions of each feature included in the blended mammogram.

Figure 36(a) shows original M56 (a blended mammogram). Figure 35(a) was obtained by global enhancement of adaptive gain processing of Deslauriers-Dubuc interpolation. Figure 34(a) shows enlarged areas containing each feature in the processed mammogram for adaptive gain of DD interpolation of contrast enhancement. For comparison of contrast, features within Figures 36(a) and 35(a) were rescaled collectively.

Figure 35(a), (b) showed enhancement of the entire mammogram, and Figure 35(c), (d) showed enhancement of the five pre-known features within the five small rectangles. Because the arbitrary rectangles enhancement can adaptively select parameters according to different features, it is more flexible than the enhancement scheme of treating all the features with the same enhancement parameters, thus enable us to enhance the features more effectively while reducing the enhancement of noise. Figure 36 shows the enhancement of an arbitrary region of interest (ROI) using adaptive gain processing of DD interpolation on an interval.

By constraining the enhancement to only the interest region, computation is greatly reduced. Table 3 shows the comparison of actual computation time of processing the entire mammogram vs only the selected ROI.

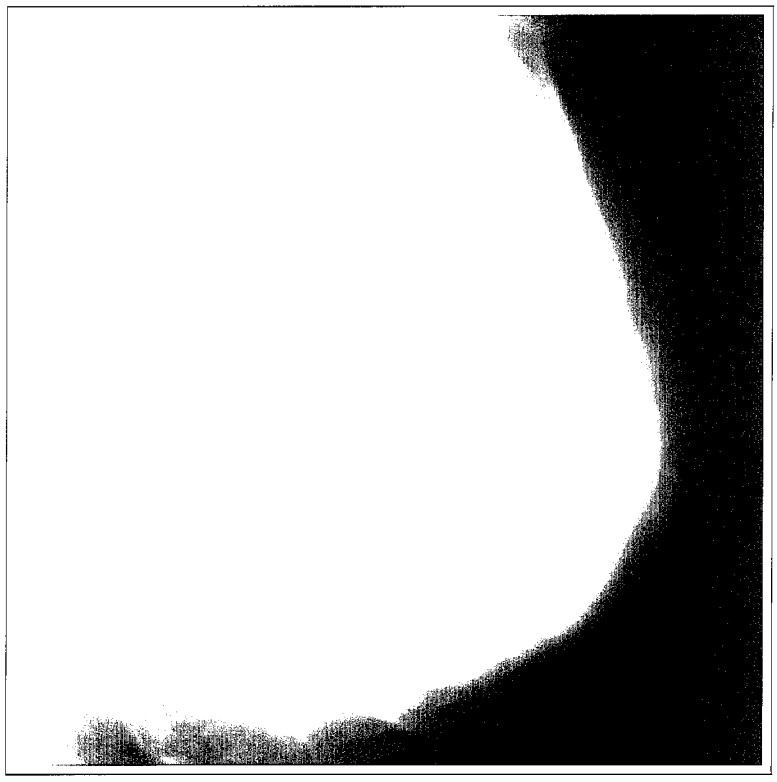

(a)

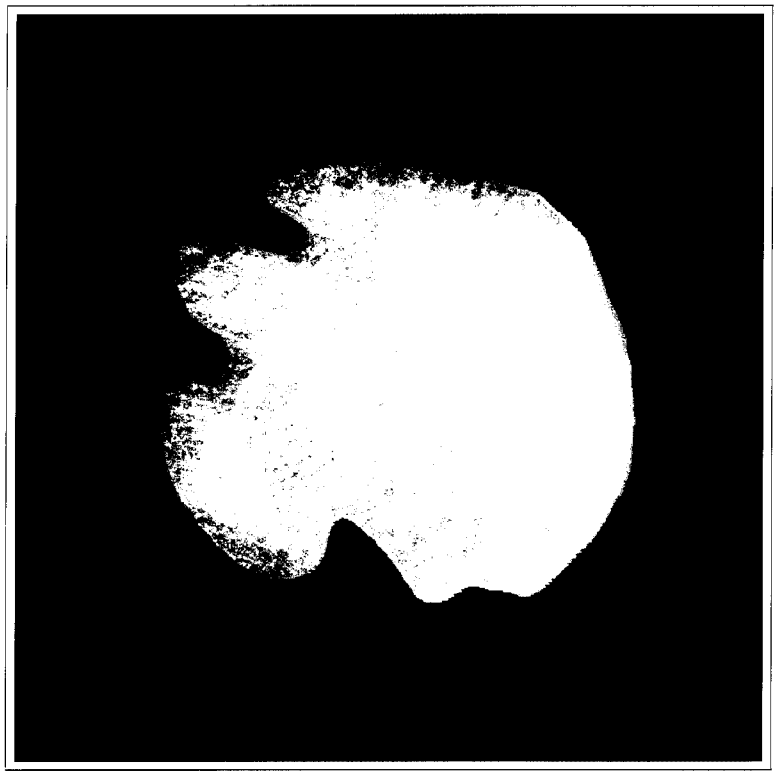

(b)

Figure 36: Blended mammogram: (a) Original mammogram blended with mathematical phantom. (b) ROI enhancement by adaptive gain processing of DD interpolation wavelet transform.

Table 3: Comparison of computation time. $T_{Entire-mammogram}$ represents the time to process a complete image matrix, while T_{ROI} represents the time to process only a selected ROI. The number of pixels within the ROI shown in Figure 12 was 76,267 (executing on Sun Sparc station 10/30).

Computation time (in seconds) comparison of whole mammogram vs ROI			
Matrix size (number of pixels)	$T_{Entire-mammogram}$	T_{ROI}	$T_{Entire-mammogram}/T_{ROI}$
512x512	748	135	5.54
1024x1024	5760	135	42.67

2.3.3 Auto-correlation shell representations

This section introduces another approach for accomplishing mammographic feature analysis by an overcomplete multiresolution representation: auto-correlation shell representation of compactly supported wavelets. We show that an arbitrary region of interest (ROI) of the mammogram can be enhanced using the auto-correlation shell. The ROI enhancement provides the radiologists a way to view the mammogram with only the ROI enhanced on the screen.

Analytical formulation for auto-correlation shells

In this section, we have investigated auto-correlation functions of Daubechies's compactly supported wavelets [36]. This representation is attractive because the shape of the basis functions for this representation are symmetric, and allow for perfect reconstruction. We have used this representation to decompose an arbitrary region of interest (ROI) within a mammogram, so that the ROI may be analyzed independently.

Since the coefficients of orthogonal wavelet expansions are not shift invariant in general, it can be quite difficult to explore the property of features from scale to scale. The asymmetric shape of compactly supported wavelets, makes these wavelets poor edge detectors, and can introduce artifacts when image enhancement is based on wavelet coefficients alone. However the compact support characteristic of these bases make them exact both in decomposition and reconstruction. The auto-correlation shell basis function has the same support width of its associated compactly supported wavelets.

To overcome the drawbacks of compactly supported orthogonal wavelets in the application of image analysis, Saito and Beylkin [36] introduced the notion of an *auto-correlation shell* . Let $\psi(x)$ be some compactly supported wavelet, and $\phi(x)$ be the scaling function. By definition of auto-correlation, we can write

$$\Phi(x) = \int_{-\infty}^{+\infty} \phi(y)\phi(y-x)dy, \qquad \Psi(x) = \int_{-\infty}^{+\infty} \psi(y)\psi(y-x)dy$$

where their respective Fourier transforms are

$$\hat{\Phi}(\xi) = |\hat{\phi}(\xi)|^2, \qquad \hat{\Psi}(\xi) = |\hat{\psi}(\xi)|^2.$$

Both $\Psi(x)$ and $\Psi(x)$ are supported within the interval $[-L+1, L+1]$, where L is the length of the quadrature mirror filter of a compactly supported orthogonal wavelet, and $\Psi(x)$ and $\Psi(x)$ are symmetric. Figure 38 and Figure 39 show the analyzing filters of the auto-correlation shell and Daubechies's wavelet with two vanishing moments.

The functions $\Psi(x)$ may be viewed as a pseudo-differential operator, this allow us to locate the edges of a signal at different scales of auto-correlation expansions. From Figure 40, we can see that the auto-correlation functions $\Phi(x)$ and $\Psi(x)$ are smoother than the functions $\phi(x)$ and $\psi(x)$, and $\hat{\Phi}(\xi)$ and $\hat{\Psi}(\xi)$ decay faster than $\hat{\phi}(\xi)$ and $\hat{\psi}(\xi)$, respectively. The auto-correlated shell basis function of Daubechies's compactly supported wavelets with $N = 2$ are shown in figure 37.

Let $\{h_k\}_{-L+1 \le k \le L-1}$ be the low pass filter related with $\Phi(x)$, and let $\{g_k\}_{-L+1 \le k \le L-1}$ be the high pass filter related to $\Psi(x)$. We have implemented a pyramid algorithm for expanding a function f into an auto-correlation shell:

$$f_{j,k} = \sum_{l=-L+1}^{L-1} h_l f_{j-1,k+2^{j-1}l}$$

$$d_{j,k} = \sum_{l=-L+1}^{L-1} g_l f_{j-1,k+2^{j-1}l}.$$

Reconstruction is accomplished by

$$f_{j-1,k} = \frac{1}{\sqrt{2}}(s_k + d_k).$$

2.3.4 Summary

In this study, methods for accomplishing adaptive contrast enhancement by multiscale representations were further investigated. Contrast enhancement was applied to features of specific interest to mammography including masses, spicules and microcalcifications. Multiresolution representations provided an adaptive mechanism for the local emphasis of such features blended into digitized mammograms. Average interpolation and Deslauriers-Dubuc interpolation representations on an interval enabled us to enhance arbitrary regions of interest within a mammogram. The enhancement of ROI's provides the radiologists an interactive way of processing only an interesting suspicious region of a mammogram, while reducing the computational cost compared to processing an entire

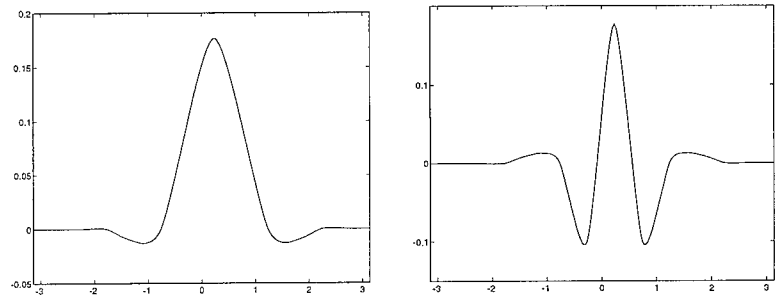

(a) (b)

Figure 37: Plots of auto-correlation functions of Daubechies's compactly supported wavelet with $L = 4$. (a) $\Phi(x)$, (b) $\Psi(x)$.

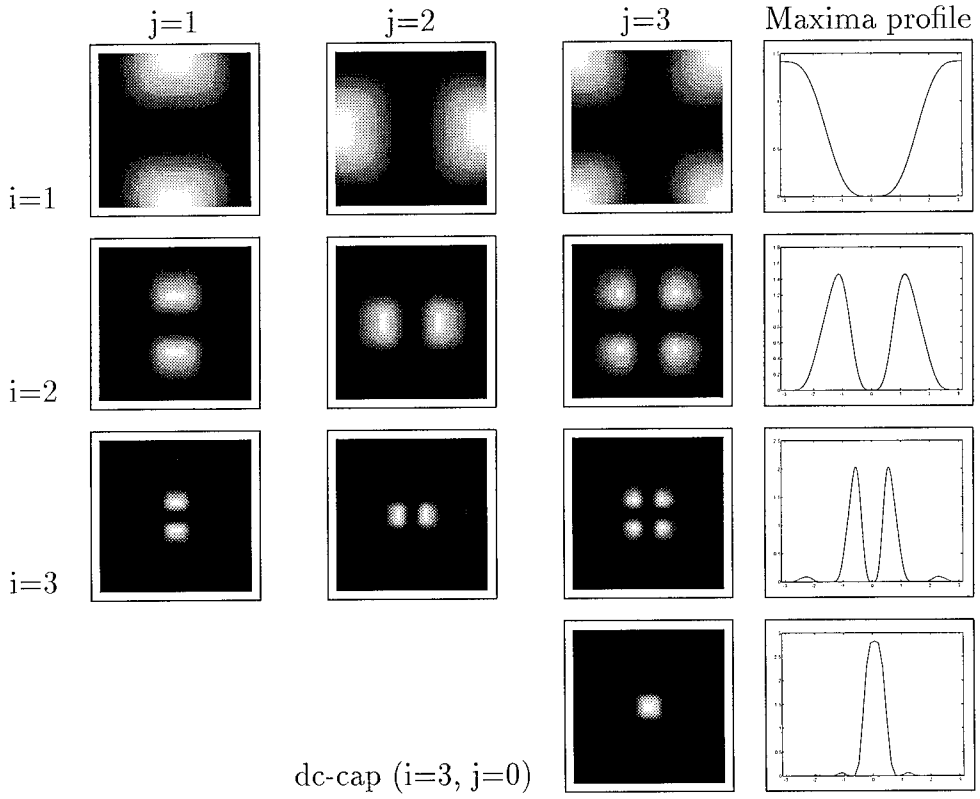

Figure 38: Analyzing filters for auto-correlation shell of Daubechies's compactly support wavelets with two vanishing moments (three levels of analysis shown).

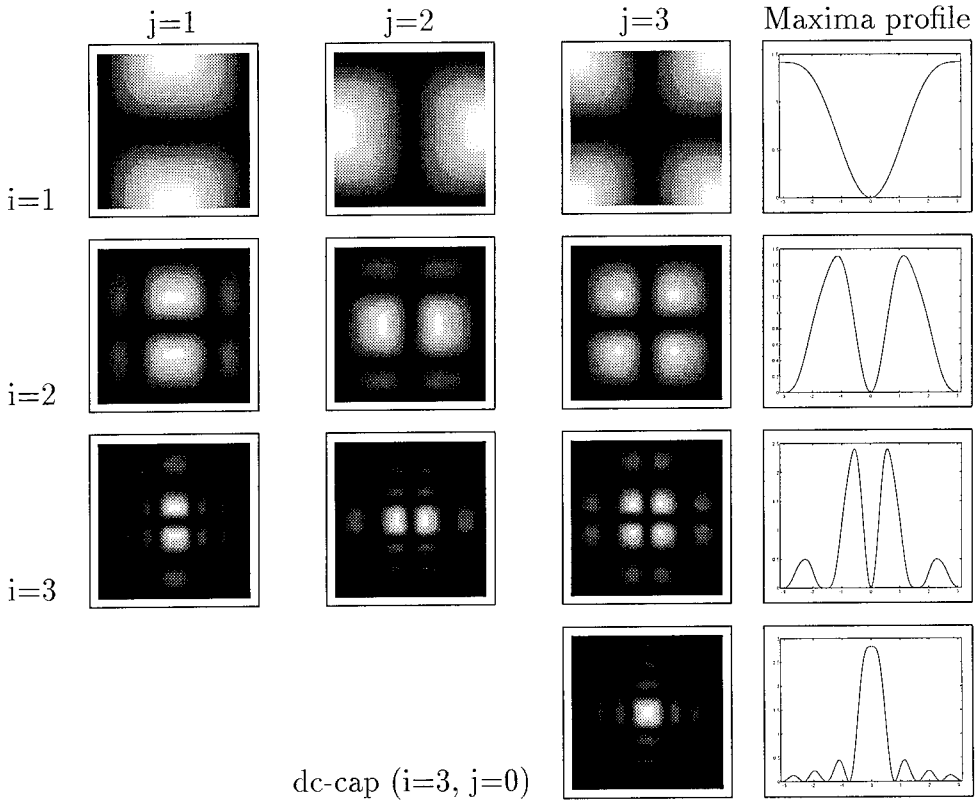

Figure 39: Analyzing filters for Daubechies's compactly supported wavelets with two vanishing moments (three levels of analysis shown).

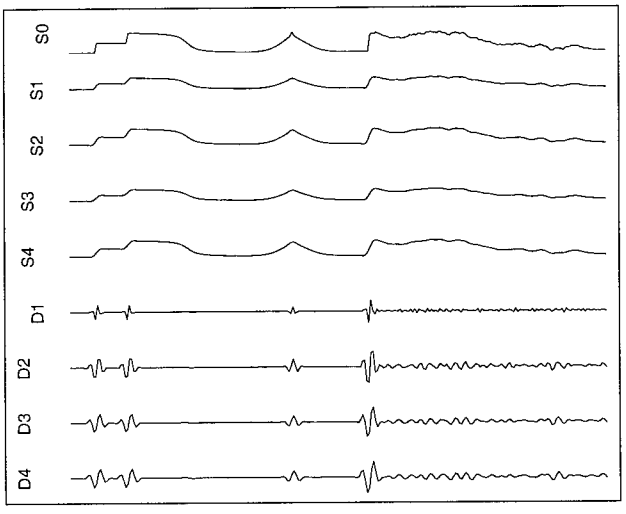

Figure 40: 1-D signal expanded with an auto-correlation shell. The locations of the edges in the original signal S_0 correspond to the zero-crossings in the detail information D_1, D_2, D_3, D_4 .

mammogram. In addition, the representation of an auto-correlation shell was studied. This representation can also be used to enhance mammographic features over an arbitrary region. These initial results are encouraging and suggest that wavelet based image processing algorithms could play an important role in improving the imaging performance of digital mammography.

2.4 Quantitative Evaluation of Clinical Images

2.4.1 Introduction

This part of the report relates to the development of objective ways to assess the performance of wavelet image processing algorithms. The objective is to develop techniques to evaluate wavelet algorithms so they can then be optimized for clinical use in mammography.

Substantial progress has been made in the development of techniques to assist in the quantitative evaluation of wavelet based image processing algorithms. In addition, these techniques have been applied to optimize the three parameters available in current wavelet based algorithms. Specific achievements in the past year include:

- a demonstration of the ability of optimized wavelet based algorithms to make visible simple objects in a noisy background which were previously invisible;
- a demonstration of the inherent superiority of wavelet based algorithms for the detection of simple objects as compared to algorithms frequently used in medical imaging including unsharp mask enhancement and median filtering;
- a demonstration of the special requirements of wavelet algorithms when enhancing the visibility of features of specific interest in mammography, namely microcalcifications, masses and fibril structures.

2.4.2 Specific projects completed

1. Image quality index. Computer simulated phantoms are an attractive choice for evaluation of image processing algorithms since the features of interest are known and well quantified. We developed a metric of the improvement in image Signal to Noise Ratio (SNR) and used an Enhancement Factor ($EF = SNR_o/SNR_i$) where the subscripts o and i refer to the processed image and original image, respectively. We validated that there was an excellent correlation between the computed EF and observer performance in psychophysics tests (see reference 1 in section 2.5).

2. Optimization of wavelet algorithms. Three separate wavelet basis functions were investigated (i.e. dyadic, hexagonal and phi). Each algorithm has three parameters (Level [L], Threshold [T], and Gain [G]) which may be varied. The effects of these three parameters on all three wavelet basis functions were systematically investigated for simple structures (e.g. Gaussian signals) embedded in white (Gaussian) noise.

   This work concluded that the three parameters have similar effects irrespective of the selected wavelet basis. In addition, the study demonstrated that wavelet based algorithms are generally not linear and that significant improvements in SNR can be achieved with optimized values of the parameters L, T and G. Another encouraging finding was that the false positive rate was generally very low provided that the gain parameter was not set too high (see references 1, 3, 6 and 9 in section 2.5).

3. Size and shape factors. Two important variables for the objects of interest in mammograms are object shape and object size. This is of particular relevance given the inherent multiscale capabilities of wavelet signal decomposition.

   The importance of shape was systematically investigated and published (see reference 3 in section 2.5) and a paper describing in detail the significance of shape will be presented at the forthcoming SPIE meeting in San Diego in February 1995 (see reference 6 in section 2.5). In general, the size of a feature of interest is more important than its specific shape. Furthermore, it is possible to optimize wavelet algorithms for any selected feature size.

4. Mammographic features. The specific objects of interest in mammograms are masses, microcalcification clusters and fibrils. The ability of wavelet based algorithms to enhance these features were investigated using both computer simulated phantoms, and physical phantoms radiographed using a screen/film combination designed for mammography and subsequently digitized to permit image processing.

   Results of these investigations have been published for both phantom images (see references 4 and 9) and for radiographs of the American College of Radiology (ACR) accreditation phantom (see reference 2 in section 2.5). These studies showed that the differing types of features investigated would benefit significantly from specially tailored algorithms.

5. Clinical applications. In addition to the phantom studies, we have performed investigations into the effectiveness of digitized clinical mammograms. These studies have generally shown that the trends identified with computer simulated physical phantoms and with radiographs of the ACR phantom are similar to those found with

clinical mammograms. The most promising wavelet basis identified by all three approaches is the dyadic basis. The enhancement strategy that shows the most promise is an Edge enhancement where it is only the wavelet maxima at a selected scale which are enhanced by a gain factor. Two alternative wavelet coefficient enhancement strategies investigated (Gain and Histogram Equalization) were generally found to be inferior to Edge enhancement. Full details of these results are available in the published papers (see references 2, 7 and 8).

2.4.3 Current projects

1. Image display. We are currently investigating ways of presenting digital mammographic images on soft copy displays. This issue is difficult because of the large matrix sizes and the number of bits used to code for any individual pixel. Our preliminary results were presented at the SPIE meeting on Medical Imaging in San Diego in February 1994 (see reference 5 in section 2.5).

2. Digital x-ray images (LoRad system). A recently installed LoRad biopsy device incorporates a small field of view high resolution (10242) digital imaging device. The clinical use of this system is to permit needle core biopsies to be obtained. We are currently using this system to radiograph images of the ACR phantom and also using clinical images. (see reference 5 in section 2.5).

3. Structured background. There are two major sources of noise in mammograms. The first arises from quantum mottle and film granularity, and this type of noise may be simulated using the computer generated phantom images as described above. A second source of "noise" is the structure patterns in mammograms. A major thrust of the work being planned is to investigate how a structured mammographic background affects the visibility of features which identify cancers (masses, microcalcifications and fibrils). In addition, the ability of wavelet based algorithms to improve feature visibility will be investigated. Of particular importance is whether algorithms optimized for random Gaussian noise are also optimized for structured background.

4. Digital mammogram databases

   We have purchased a Mammographic database from the Mammographic Image Analysis Society in England with consists of 322 images digitized with a 50 micrometer spots size. In addition, we are in the process of digitizing a collection of biopsy proven cases from the University of Florida to use for evaluation in our studies of wavelet analysis.

5. Wavelet compression

   We are in the process of developing methods for applying wavelet and jpeg compression to mammograms with the intention of evaluating both methods for the best compression method for these large image files. Receiver Operator Characteristic (ROC) analysis as well as forced choice analysis will be carried out to determine the best method and the limits of compression.

6. Sampling images for display

   We are beginning the investigation of subsampling methods for reducing image matrix size for digital mammographic images. We will evaluate methods using Receiver Operating Characteristics and forced choice analysis as well as physical measurements to determine the best clinical way to subsample as well as to develop methods for correlating physical measurements with clinical accuracy.

7. Mammography database

   We are updating the mammography database to meet the American College of Radiology's new rules for outcomes reporting.

2.5 Published journal papers and conference proceedings

1. Xing Y, Huda W, Laine A, Fan J "Simulated phantom images for optimizing wavelet based image processing algorithms in mammography" Proceedings of the SPIE, San Diego, 25-26 July 1994, Volume 2299 207-217.

2. Qu G, Huda W, Laine A, Steinbach BG, Honeyman JC "Use of accreditation phantoms and clinical images to evaluate mammography image processing algorithms" In Digital Mammography, Editors AG Gale et al, Elsevier Science BV; Amsterdam (1994) 345- 354.

3. Jing Z, Zheng Y, Huda W, Laine A and Fan J "Mathematical models for quantitative evaluation of wavelet based image processing algorithms" Proceedings of the SPIE, San Diego, 25-26 July 1994, SPIE Volume 2303 569-578.

4. Laine A, Schuler S, Fan J and Huda W "Mammographic feature enhancement by multiscale analysis", IEEE Transactions on Medical Imaging, Vol. 13, No.4, December, 1994.

5. Honeyman JC, Chen D, Huda W and Steinbach BG "Impact of image display parameters on the visibility of microcalcifications and masses" Submitted to the SPIE.

6. Huda W, Xing Y, Lain A, Fan J, Steinbach BG and Honeyman JC "Assessment of a wavelet image processing algorithm for mammography" Submitted to SPIE.

7. Steinbach BG, Laine A, Huda W and Honeyman JC "Mammography image enhancement by using wavelet transforms" Submitted to RadioGraphics.

8. Laine A, Huda W, Steinbach BG and Honeyman JC "Mammographic image processing using wavelet processing techniques" submitted to European Radiology.

9. Xing Y, Huda W, Laine A and Fan J "Optimization of a dyadic wavelet for mammography" In preparation for submission to IEEE Transactions on Medical Imaging.

2.6 Published abstracts and presentations

1. Title: Use of phantoms and clinical images to evaluate wavelet based image processing algorithms in mammography.

   Authors: G Qu, W Huda, A Laine, BG Steinbach and JC Honeyman.

   Presented at the 1994 American Association of Physicists in Medicine (AAPM) meeting in Anaheim, CA

   Abstract: Wavelet based image processing algorithms have been proposed to enhance clinically important features in mammograms. In this study, images of an ACR mammographic phantom and clinical images were both used to evaluate the subjective improvement of image quality. Readers were asked to compare the visibility of masses, spicules and microcalcifications of images processed using nine different wavelet algorithms. The visibility rankings ranged from a value of 1 (markedly less than the original) to 5 (markedly better than the original). For the ACR phantom images, a wide range of positive and negative rankings were obtained suggesting that algorithms could be very good or very bad. For clinical images, however, most rankings tended to correspond to the mean value. The advantages and limitations of each phantom will be discussed.

2. Title: Investigation of wavelet based image processing algorithms for use in mammography

   Authors: Y Zheng, Y Xing, W Huda and A Laine.

   Presented at the 1994 American Association of Physicists in Medicine (AAPM) meeting in Anaheim, CA

   Abstract: It is important to optimize image processing algorithms prior to subjecting them to clinical evaluation. In this study, computer simulated phantoms were used to systematically investigate the parameters of wavelet image processing algorithms. These included the hierarchical decomposition level, wavelet coefficient thresholds and enhancement gain values [Laine et al, SPIE Volume 1905 (1993) 521-532)]. Image processing algorithms designed for use in mammography were applied to these computer generated images and the input/output SNR values determined as a function of each parameter. This methodology permits the identification of promising wavelet parameters which could permit mammograms to be processed to improve the visibility of features such as masses, spiculations and microcalcifications.

3. Title: Assessment of contrast enhancement for wavelet based mammography image processing algorithms.

   Authors: W Huda, A Laine, JC Honeyman, BG Steinbach.

   Presented at the 1994 Canadian Organization of Medical Physics (COMP) meeting in Toronto

   Abstract: Wavelet based image enhancement algorithms have been proposed for use in mammography to improve visibility of clinically important features. In this study, three wavelet based algorithms were evaluated for their ability to enhance the visibility of masses, spicular lesions and microcalcifications which had been mathematically blended into digitized clinical mammograms. The results were compared with a competitive local enhancement (unsharp masking) algorithm. Contrast Improvement Indices (CIIs) were obtained by measuring the ratio of contrast in the processed image to that of the original image. For the wavelet algorithms investigated, CII values were in the range 1.9 to 4.5 for the three types of added mammographic feature. The corresponding CII values for the unsharp mask algorithm, however, were in the range 1.1 to 1.8. The results of this study indicate that wavelet based image processing algorithms could be useful for enhancing clinical mammograms.

4. Title: Mammography image enhancement using wavelet transforms.

   Authors: BG Steinbach, A Laine, JC Honeyman, W Huda.

   Presented at the meeting of the American Rontgen Ray Society

   Abstract: We present a novel approach for accomplishing mammographic feature analysis utilizing wavelet transforms. Identification of image features at different scales permits selected attributes in a mammogram to be enhanced. Using digitized mammograms, wavelet transform algorithms were evaluated in several cases of biopsy proven breast carcinomas. Spiculated and well defined masses of varying degrees of subtlety were processed using image processing algorithms based on multiscale wavelet transforms. For comparison purposes, these images were also processed using traditional histogram equalization.

   Mammograms processed with algorithms based on the wavelet transform showed some improvements in feature visualization. This Wavelet Transform method has the potential to significantly improve the visibility of clinically important features (i.e. masses, spicules & microcalcifications) and merits further investigation.

5. Title: Assessment of a wavelet image processing algorithm for mammography.

   Authors: W Huda, Y Xing, A Laine, J Fan, BG Steinbach, JC Honeyman.

   Submitted to: Image Processing, Murray H Loew, at M195 Medical Imaging 1995, 26 February - 2 March 1995, San Diego

   Purpose: Image processing algorithms based on the wavelet transform has been proposed to improve the visibility of mammographic features. In this study, a computer simulated phantom was used to optimize a dyadic wavelet algorithm. The degree of image enhancement achieved with this algorithm was compared with algorithms currently used in diagnostic radiology.

   Method: A computer simulated phantom was generated which contained masses, fibrils and microcalcifications together with added random noise. Image improvement was determined from the ratio of output to input signal to noise ratios. Performance of the following three algorithms was investigated: 1) dyadic wavelet transform; 2) unsharp masking; 3) median filtering.

   Results: Each algorithm has several free parameters which may be altered and affect the degree of image enhancement achieved. The properties of these parameters for each algorithm were studied. Optimal parameters for these algorithms were found to

depend on the type of mammographic feature being studied.

Conclusions: The results obtained show that a multiresolution approach to mammographic image processing using a dyadic wavelet transform is generally a more powerful tool than those offered by traditional image processing algorithms.

6. Title: Impact of image display parameters on the visibility of microcalcifications and masses.

Authors: JC Honeyman, D Chen, W Huda, BG Steinbach.

Submitted to: Image Display, Yongmin Kim, at M195 Medical Imaging 1995, 26 February - 2 March 1995, San Diego

Purpose: High resolution digital mammography systems are likely to appear in clinical practice in the near future. Digital image data will permit the manner in which mammograms are displayed to be readily modified. In this study, the importance of display parameters on mammography feature conspicuity was evaluated using images printed on film and displayed on diagnostic workstations.

Method: Clinical mammographic images, 5 x 5 cm in size, were obtained from a LoRad Digital Spot Mammography system. The image matrix size was 5122 with a pixel dimension of about 100 em. Ten images had microcalcifications and ten images had masses. For each image, nine copies were made with differing window and level settings which were printed on film and displayed on a monitor. Five radiologists specializing in mammography ranked conspicuity of each mammographic feature from the least visible to the most visible in a 9 forced choice experiment.

Results: The characteristic curves for transforming image pixel intensity to optical density (film) and image monitor intensity (workstations) were obtained. The significance of window and level on the perceived visibility of mammographic features were determined. There are differences between small high contrast features such as mammographic calcifications and larger low contrast features such as malignant masses. The relative ranking of the conspicuity of mammographic features, however, were generally similar for both film and workstation displays.

Conclusions: The data obtained quantify the significance of image display parameters for improving the conspicuity of mammographic features. These results will permit the optimization for printing films from digital mammography data and assist in the design of display workstations for use in mammography.

2.7 Lectures and invited talks

1. Andrew Laine, International Conference of the IEEE Engineering in Medicine and Biology Society (EMBS), November 1-2, 1994, Baltimore, MD, Invited speaker.

2. Andrew Laine, Yale University, Department of Mathematics, Colloquium guest speaker, April, 1994.

3. Andrew Laine, University of Chicago, Departments of Computer Science and Radiology, Invited lectures, Colloquium speaker, January, 1994.

3 Conclusions

During the past year, we have made significant progress in the development of a methodology for accomplishing adaptive contrast enhancement by multiscale representations. Our studies have demonstrated that features extracted from multiresolution representations can provide an adaptive mechanism for the local emphasis of salient and subtle features of importance to mammography. The improved contrast of mammographic features make these techniques appealing for computed aided diagnosis (CAD) and screening mammography. Screening mammography examinations are certain to grow substantially in the next few years, and analytic methods that can assist general radiologists in reading mammograms shall be of great importance.

In the paragraphs below, we summarize our progress and identify future directions of research to be carried out during the next year of our investigation.

We have established connections between dyadic wavelet enhancement algorithms and traditional unsharp masking. We proved that two cases of linear enhancement were mathematically equivalent to traditional unsharp masking with Gaussian low-pass filtering. We designed a methodology for nonlinear enhancement with a simple nonlinear function to overcome the dynamic range requirement usually associated contrast enhancement of digital radiographs. By careful selection of wavelet filters and enhancement function, we showed that artifacts can be eliminated. An additional advantage of our simple enhancement function is that it includes traditional unsharp masking as a subset. We showed how an edge-preserved denoising stage (wavelet shrinkage) can be appropriately incorporated into our contrast enhancement framework, and introduced a method for adaptive threshold estimation. We showed how denoising and enhancement operations should be carried out for two dimensional images to avoid orientation distortions.

Our future research plans include the systematic study of gain and threshold parameters for the nonlinear enhancement. In addition, in the next year we shall seek localized and complex nonlinear methods to improve the performance of our existing algorithm.

We have design and implemented an interactive image editor for digital mammography, called "Xmam". We have defined the functionality and data structures of a computer image editor that can allow radiologists to interactively indicate on a computer screens (simultaneously displaying four radiographic views of screening) regions diagnosed as probable cancer. This tool shall facilitate the compilation of a large database of diagnosed cases to provide ground truth for the development and verification of our computer algorithms for the detection of breast cancer.

During the next year, XMam shall evolve into a front-end for our state-of-the-art mammography workstation as additional software is developed and we migrate our system onto more sophisticated hardware.

In addition, methods for accomplishing adaptive contrast enhancement by multiscale representations were further investigated. Contrast enhancement was applied to features of importance to mammography including masses, spicules and microcalcifications. Multiresolution representations provided an adaptive mechanism for the local emphasis of such features blended into digitized mammograms. Average interpolation and Deslauriers-Dubuc interpolation representations on an interval enabled us to enhance arbitrary regions of interest within digital mammograms.

Enhancement of arbitrarily shaped ROI's provides the radiologist with an interactive capability to process only suspicious regions of a mammogram, while significantly reducing execution time compared to processing an entire image matrix. In addition, the representation of an auto-correlation shell was studied. We remain excited about this representation and plan to further study its ability to enhance mammographic features over arbitrary regions. These initial results are encouraging and suggest that wavelet based image processing algorithms shall play an important role in improving the imaging performance of digital mammography.

Finally, we reported on the development of objective ways to assess the performance of wavelet image processing algorithms. Our objective is to develop techniques to evaluate wavelet algorithms so they can then be optimized for clinical use in mammography.

Substantial progress was made in the development of techniques to assist in the quantitative evaluation of wavelet based image processing algorithms. In addition, these techniques were applied to optimize the three parameters available in current wavelet based algorithms.

During the next year, we expect to continue our study of wavelet filter design and selection in the refinement of our early basis functions (dyadic wavelets, phi-transform, and hexagonal wavelets) conceived as initial instances in the evolution of three *specialized detectors*. As described in our research plan, we shall design three "detectors" to focus on three distinct types of mammographic features: (1) microcalcifications, (2) spicular lesions and (3) masses.

In summary, we have exceeded the goals as described in our Statement of Work for the second year, and our research and development plans remain on schedule.

References

[1] A.G. Haus and M.J. Yaffe, Eds., *A categorical course in physics. Technical aspects of breast imaging.* Radiological Society of North America, 1993, Presented at the 79^{th} scientific assembly and annual meeting of the RSNA.

[2] S.A. Feig and R.E. Hendrick, "Risk, benefit and controversy in mammographic screening", in *A categorical course in physics. Technical aspects of breast imaging*, A.G. Haus and M.J. Yaffe, Eds. Radiological Society of North America, 1993, pp. 119–135, Presented at the 79^{th} scientific assembly and annual meeting of the RSNA.

[3] R.A. Smith, "Epidemiology of breast cancer", in *A categorical course in physics. Technical aspects of breast imaging*, A.G. Haus and M.J. Yaffe, Eds. Radiological Society of North America, 1993, pp. 21–33, Presented at the 79^{th} scientific assembly and annual meeting of the RSNA.

[4] G.T. Barnes and G.D. Frey, Eds., *Screen film mammography. Imaging considerations and medical physics responsibilities*, Madison, Wisconsin, 1991. Medical Physics Publishing.

[5] P.C. Johns and M.J. Yaffe, "X-ray characterization of normal and neoplastic breast tissues", *Physics in Medicine and Biology*, vol. 32, no. 6, pp. 675–695, Feb. 1987.

[6] M.J. Yaffe, R.J. Jennings, R. Fahrig, and T.R. Fewell, "X-ray spectral considerations for mammography", in *A categorical course in physics. Technical aspects of breast imaging*, A.G. Haus and M.J. Yaffe, Eds. Radiological Society of North America, 1993, pp. 63–72, Presented at the 79^{th} scientific assembly and annual meeting of the RSNA.

[7] I. Brodie and R.A. Gutcheck, "Radiographic information theory and application to mammography", *Medical Physics*, vol. 9, 1982.

[8] T.N. Wiesel, "Postnatal development of the visual cortex and the influence of environment", *Nature*, vol. 299, no. 5883, pp. 583–591, Oct. 1982.

[9] D.C. Wang, A.H. Vagnucci, and C.C. Li, "Digital image enhancement: a survey", *Computer Vision, Graphics, and Image Processing*, vol. 24, pp. 363–381, 1983.

[10] R. Hummel, "Histogram modification techniques", *Computer Graphics and Image Processing*, vol. 4, pp. 209–224, 1975.

[11] W. Frei, "Image enhancement by histogram hyperbolization", *Computer Graphics and Image Processing*, vol. 6, pp. 286–294, 1977.

[12] S.M. Pizer, E.P. Amburn, J.D. Austin, R. Cromartie, A. Geselowitz, T. Greer, B.T.H. Romeny, J.B. Zimmerman, and K. Zuiderveld, "Adaptive histogram equalization and its variations", *Computer Vision, Graphics, and Image Processing*, vol. 39, pp. 355–368, 1987.

[13] A. Rosenfeld and A.C. Kak, *Digital picture processing*, Academic Press, Second edition, New York, USA, 1982.

[14] L.D. Loo, K. Doi, and C.E. Metz, "Investigation of basic imaging properties in digital radiograpgy. 4. effect of unsharp masking on the detectability of simple patterns", *Medical Physics*, vol. 12, no. 2, pp. 209–214, Mar. 1985.

[15] F. Neycenssac, "Contrast enhancement using the laplacian-of-a-gaussian filter", *CVGIP: Graphical Models and Image Processing*, vol. 55, no. 6, pp. 447–463, 1993.

[16] R. Gordon and R.M. Rangayan, "Feature enhancement of film mammograms using fixed and adaptive neighborhood", *Applied Optics*, vol. 23, pp. 560–564, 1984.

[17] A. Beghdadi and A.L. Negrate, "Contrast enhancement technique based on local detection of edges", *Computer Vision, Graphics, and Image Processing*, vol. 46, pp. 162–174, 1989.

[18] A. Laine, "Multiscale wavelet representations for mammographic feature analysis", in *Image Enhancement Techniques: Computer Science. National Cancer Institute Breast Imaging Workshop: State-of-the-Art and New Technologies*, Bethesda, Maryland, Sept. 1991.

[19] A. Laine and S. Song, "Multiscale wavelet representations for mammographic feature analysis", in *Proceedings of SPIE. Conference on Mathematical Methods in Medical Imaging*, San Diego, California, July 1992.

[20] A. Laine and S. Song, "Wavelet processing techniques for digital mammography", in *Proceedings of SPIE. Conference on Visualization in Biomedical Computing*, Chapel Hill, North Carolina, Oct. 1992.

[21] A. Laine, S. Song, and J. Fan, "Adaptive multiscale processing for contrast enhancement", in *Proceedings of SPIE. Conference on Biomedical Imaging and Biomedical Visualization*, San Jose, California, Feb. 1993.

[22] B.D. Jawerth, M.L. Hilton, and T.L. Huntsberger, "Local enhancement of compressed images", *Journal of Mathematical Imaging and Vision*, vol. 3, pp. 39–49, 1993.

[23] A. Laine, S. Schuler, J. Fan, and W. Huda, "Mammographic feature enhancement by multiscale analysis", *IEEE Transaction on Medical Imaging*, vol. 13, no. 14, Dec. 1994.

[24] J. Lu and D.M. Healy Jr, "Contrast enhancement of medical images using multiscale edge representation", in *Proceedings of SPIE: Wavelet applications*, Orlando, Florida, Apr. 1994.

[25] D.L. Donoho, "Nonlinear wavelet methods for recovery of signals, densities, and spectra from indirect and noisy data", in *Proceedings of Symposia Applied Mathematics*, 1993, vol. 00, pp. 173–205.

[26] S. Mallat and Sifen Zhong, "Characterization of signals from multiscale edges", *IEEE Transactions on Pattern Analysis and Machine Intelligence*, vol. 14, no. 7, pp. 710–732, July 1992.

[27] S. Mallat and W.L. Hwang, "Sigularity detection and processing with wavelets", *IEEE Transactions on Information Theory*, vol. 38, no. 2, pp. 617–643, Mar. 1992.

[28] H. Voorhees and T. Poggio, "Tetecting textons and texture boundaries in natural images", in *Proceedings of First International Conference on Computer Vision*, Apr. 1987, pp. 250–258.

[29] M.L. Giger, "Computer-aided diagonosis", in *A categorical course in physics. Technical aspects of breast imaging*, A.G. Haus and M.J. Yaffe, Eds. Radiological Society of North America, 1992, pp. 257–270, Presented at the 78^{th} scientific assembly and annual meeting of the RSNA.

[30] Carl J. Vyborny, "Can computers help radiologists read mammograms?", *Radiology*, vol. 191, no. 2, pp. 315–316, May 1994.

[31] D.L. Donoho, *Recent Advances in Wavelet Analysis*, Academic Press , Inc., Boston, MA, 1994.

[32] S. Dubuc, "Interpolation through an interactive scheme", *Journal of Mathematical Analysis and Applications*, vol. 114, pp. 185–204, 1986.

[33] G. Deslauriers and S. Dubuc, "Symmetric iterative interpolation process", *Constructive Approximation*, vol. 5, pp. 49–68, 1989.

[34] A. Cohen and I. Daubechies, "Wavelets on the interval and fast wavelet transforms", *Applied and Computational Harmonic Analysis*, vol. 1, no. 1, pp. 54–81, 1993.

[35] W.M. Morrow, R.B. Paranjape, R.M. Rangayyan, and J.E.L. Desautels, "Region-based contrast enhancement of mammograms", *IEEE Transactions on Medical Imaging*, vol. 11, no. 3, pp. 392–406, Sept. 1992.

[36] N. Saito and G. Beylkin, "Multiresolution representations using auto-correlation functions of compactly supported wavelets", *Special Issue of IEEE Transactions on Signal Processing, Wavelets and Signal Processing*, 1992.

[37] S. Mallat, "A theory for multiresolution signal decomposition : the wavelet representation", *IEEE Transactions on Pattern Analysis and Machine Intelligence*, vol. 11, no. 7, pp. 674–693, July 1994.